frontiers in Cell and Developmental Biology

ORIGINAL RESEARCH
published: 25 January 2021
doi: 10.3389/fcell.2020.616878

miRNA and mRNA Profiling Links Connexin Deficiency to Deafness via Early Oxidative Damage in the Mouse *Stria Vascularis*

Giulia Gentile[1], Fabiola Paciello[2,3], Veronica Zorzi[4,5], Antonio Gianmaria Spampinato[1,6], Maria Guarnaccia[1], Giulia Crispino[5], Abraham Tettey-Matey[5], Ferdinando Scavizzi[5], Marcello Raspa[3], Anna Rita Fetoni[3,4], Sebastiano Cavallaro[1] and Fabio Mammano[5,7]**

[1] Department of Biomedical Sciences, National Research Council (CNR) Institute for Biomedical Research and Innovation, Catania, Italy, [2] Department of Neuroscience, Università Cattolica del Sacro Cuore, Rome, Italy, [3] Fondazione Policlinico Universitario A. Gemelli Istituto di Ricovero e Cura a Carattere Scientifico (IRCCS), Rome, Italy, [4] Department of Head and Neck Surgery, Università Cattolica del Sacro Cuore, Rome, Italy, [5] Department of Biomedical Sciences, National Research Council (CNR) Institute of Biochemistry and Cell Biology, Rome, Italy, [6] Department of Mathematics and Computer Science, University of Catania, Catania, Italy, [7] Department of Physics and Astronomy "G. Galilei", University of Padua, Padua, Italy

OPEN ACCESS

Edited by:
Cornelia Braicu,
Iuliu Haţieganu University of Medicine and Pharmacy, Romania

Reviewed by:
Jinsei Jung,
Yonsei University, South Korea
Jiann-Jou Yang,
Chung Shan Medical University, Taiwan

***Correspondence:**
Anna Rita Fetoni
annarita.fetoni@unicatt.it
Fabio Mammano
fabio.mammano@unipd.it

Specialty section:
This article was submitted to Molecular Medicine, a section of the journal Frontiers in Cell and Developmental Biology

Received: 13 October 2020
Accepted: 10 December 2020
Published: 25 January 2021

Citation:
Gentile G, Paciello F, Zorzi V, Spampinato AG, Guarnaccia M, Crispino G, Tettey-Matey A, Scavizzi F, Raspa M, Fetoni AR, Cavallaro S and Mammano F (2021) miRNA and mRNA Profiling Links Connexin Deficiency to Deafness via Early Oxidative Damage in the Mouse Stria Vascularis. Front. Cell Dev. Biol. 8:616878. doi: 10.3389/fcell.2020.616878

Pathogenic mutations in the non-syndromic hearing loss and deafness 1 (DFNB1) locus are the primary cause of monogenic inheritance for prelingual hearing loss. To unravel molecular pathways involved in etiopathology and look for early degeneration biomarkers, we used a system biology approach to analyze Cx30$^{-/-}$ mice at an early cochlear post-natal developmental stage. These mice are a DFNB1 mouse model with severely reduced expression levels of two connexins in the inner ear, Cx30, and Cx26. Integrated analysis of miRNA and mRNA expression profiles in the cochleae of Cx30$^{-/-}$ mice at post-natal day 5 revealed the overexpression of five miRNAs (miR-34c, miR-29b, miR-29c, miR-141, and miR-181a) linked to apoptosis, oxidative stress, and cochlear degeneration, which have Sirt1 as a common target of transcriptional and/or post-transcriptional regulation. In young adult Cx30$^{-/-}$ mice (3 months of age), these alterations culminated with blood barrier disruption in the *Stria vascularis* (*SV*), which is known to have the highest aerobic metabolic rate of all cochlear structures and whose microvascular alterations contribute to age-related degeneration and progressive decline of auditory function. Our experimental validation of selected targets links hearing acquisition failure in Cx30$^{-/-}$ mice, early oxidative stress, and metabolic dysregulation to the activation of the Sirt1–p53 axis. This is the first integrated analysis of miRNA and mRNA in the cochlea of the Cx30$^{-/-}$ mouse model, providing evidence that connexin downregulation determines a miRNA-mediated response which leads to chronic exhaustion of cochlear antioxidant defense mechanisms and consequent *SV* dysfunction. Our analyses support the notion that connexin dysfunction intervenes early on during development, causing vascular damage later on in life. This study identifies also early miRNA-mediated biomarkers of hearing impairment, either inherited or age related.

Keywords: connexins, molecular pathway analysis, early degeneration, systems biology, hearing loss, vascular dysfunction, post-natal development, oxidative stress

INTRODUCTION

Cx26 and Cx30 are the prevailing gap junction proteins in the duct of the developing and mature mammalian cochlea (Mammano, 2019). Pathogenic mutations in the *DFNB1* locus, which contains both genes (*GJB2/CX26* and *GJB6/CX30*) encoding these connexins, are the primary cause of monogenic inheritance for prelingual deafness. It remains unclear if their coordinated expression is due to digenic inheritance or mutations affecting *cis*-regulatory elements that in turn influence *GJB2/CX26* expression (Del Castillo and Del Castillo, 2017).

Knockout mouse models confirmed the essential role of inner ear connexins for hearing, since their absence causes profound deafness associated with apoptotic processes within the developing organ of Corti (OC) (Teubner et al., 2003). *Cx30* homozygous knockout-LacZ mice ($Gjb6^{tm1Kwi}/Gjb6^{tm1Kwi}$; MGI:2447863; EM:00323), hereafter abbreviated as $Cx30^{-/-}$, are a model for humans in which large deletions in the DFNB1 locus lead to downregulation of both *GJB2/CX26* and *GJB6/CX30* and profound deafness. $Cx30^{-/-}$ mice exhibit (i) severe constitutive hearing impairment with degeneration of cochlear sensory epithelium from post-natal day 18 (P18) onwards, (ii) absence of endocochlear potential (Teubner et al., 2003), and (iii) defects of the endothelial barrier in capillaries of the *stria vascularis* (*SV*) (Cohen-Salmon et al., 2007). In addition, massive downregulation of Cx26, at both mRNA and protein levels, was reported in the developing OC of $Cx30^{-/-}$ mice at P5 in non-sensory cells located between outer hair cells and *SV* (Ortolano et al., 2008); both transcript and protein levels of Cx26 were similarly reduced in the cochleae of $Cx30^{-/-}$ mice at P30 (Boulay et al., 2013).

The coordinated regulation of Cx26 and Cx30 expression in the cochlea apparently occurs as a result of NFκB pathway signaling, as it could be inhibited by expressing a stable form of the IκB repressor protein that prevents the activation/translocation of NFκB (Ortolano et al., 2008). The amplitude and duration of Ca^{2+} signals control differential activation of NFκB (Dolmetsch et al., 1998), and prior works linked alterations of Ca^{2+} signaling to hearing loss in transgenic mice (Schutz et al., 2010; Rodriguez et al., 2012). Other published data linked defective hearing acquisition to impairment of ATP- and IP_3-dependent Ca^{2+} signaling in non-sensory cells of the developing cochlea (Ceriani et al., 2016), identified inner ear connexins as both targets and effectors of these signaling mechanisms, and support the notion that connexin dysfunction intervenes early on during development, calling for a timely therapeutic intervention (Crispino et al., 2011).

Recently, the emerging role of microRNAs (miRNAs) in post-transcriptional gene expression regulation has also been investigated using knockout mouse models whose miRNA deregulated profiles may suggest a potential contribution to cochlear pathogenesis (Elkan-Miller et al., 2011; Patel and Hu, 2012; Ushakov et al., 2013; Zhang et al., 2013; Mahmoodian sani et al., 2016; Mittal et al., 2019). In addition, deficiency of Cx26 in *Gjb2/Cx26* conditional knockout mice was linked to an impaired miRNA-mediated intercellular communication through cochlear gap junctions (Zhu et al., 2015).

Here, we explored mechanisms underlying the etiopathogenesis of DFNB1 by performing an integrated genomics analysis of miRNA and mRNA expression profiles in $Cx30^{-/-}$ mice. In a prior work, transcriptomic profiles of $Cx30^{-/-}$ mice (and their wild-type siblings) were obtained at P13, highlighting a significant downregulation of betaine homocysteine *S*-methyltransferase (*Bhmt*) restricted to the *SV*, followed by the consequent local increase of homocysteine level and endothelial barrier dysfunction (Cohen-Salmon et al., 2007). In this study, we extended those results by also investigating miRNA-mediated regulation at an earlier stage of cochlear development, i.e., P5, and so looking for early degeneration biomarkers.

MATERIALS AND METHODS

Electronic Laboratory Notebooks Were Not Used.

Animals and Genotyping

Animals (*Mus musculus*) used in this study and bred at the National Research Council–Institute of Biochemistry and Cell Biology (CNR-IBBC), Infrafrontier/ESFRI–European Mouse Mutant Archive (EMMA), specific pathogen-free (SPF) barrier unit (Monterotondo Scalo, Rome, Italy), were housed in individually ventilated caging systems (Tecniplast, Gazzada, Italy) at a temperature (T) of 21 ± 2°C and relative humidity (RH) of 55 ± 15% with 50–70 air changes per hour (ACH) and under controlled (12:12 h) light–dark cycle (7 am−7 pm). Mice had *ad libitum* access to water and a standard rodent diet (Emma 23, Mucedola, Settimo Milanese, Italy). Both male and female homozygous $Cx30^{-/-}$ [EMMA ID (EM):00323] pups at P5, as well as their wild-type P5 siblings ($Cx30^{+/+}$), were used. The background strain of these mice was C57BL/6J.

Primer pairs for $Cx30^{-/-}$ mice were specific for the wild-type alleles:

f: 5′-GGTACCTTCTACTAATTAGCTTGG-3′,

r: 5′-AGGTGGTACCCATTGTAGAGGAAG-3′.

To visualize the deletion, primers specific for the lacZ region (which flanks the deleted allele) were used in combination with the corresponding wild-type forward primer:

lacZ 5′-AGCGAGTAACAACCCGTCGGATTC-3′.

Study Design

To construct the optimal experimental design and estimate the minimum number of animals necessary for the experiments (sample size of the groups), for each type of experiment and for each genetically modified and control strain, we set probability $a = 5\% = 0.05$ for the type I error in the *t*-test. Then, fixing $b = 4a = 20\% = 0.2$ to obtain a test power of $1–b = 80\% = 0.8$, we computed the number n of each of the two samples to be compared using the following formula:

Abbreviations: ARHL, Age-related hearing loss; DEG, Differentially expressed gene; DFNB1, Non-syndromic hearing loss and deafness 1; ER, Endoplasmic reticulum; GO, Gene ontology; GEO, Gene Expression Omnibus; m, Post-natal month; MAM, Mitochondria-associated membrane; miRNA, MicroRNA; OC, Organ of Corti; P, Post-natal day; PPI, Protein–protein interaction; SERCA, Sarcoplasmic/endoplasmic reticulum calcium ATPase; *SV*, *Stria vascularis*.

$$n > 2\left[\frac{\left(z_{\alpha/2} + z_{\beta}\right) \cdot \sigma^2}{\Delta}\right] \quad (1)$$

with $z_{a/2} = 1.96$ and $z_b = 0.842$. Based on experiments of the same type carried out in prior work, we quantified the variability of the data (variance, σ^2) and established the minimum difference, $\Delta = |\mu_1\text{-}\mu_2|$, between averages that had a biological significance. To minimize subjective bias, sample identity (e.g., genotypes) was randomized by associating an identification number to each sample before processing. One sample was excluded from the analysis after microarray quality control in miRNA expression profiling.

RNA Extraction and Evaluation

To study gene expression regulation by miRNAs during cochlear development in Cx30$^{-/-}$ mice, we performed an integrated functional genomics analysis (for data analysis flow chart, see **Supplementary Figure 1**). We used both cochleae of $n = 4$ mice at P5 for each of the two genotypes and extracted total RNA, including miRNAs using the Qiagen miRNeasy Mini Kit (Qiagen, Hilden, Germany). The quality of RNA was evaluated with Agilent 2100 Bioanalyzer, using the Small RNA assay for miRNAs and the RNA 6000 Nano assay for mRNAs. All of the eight samples thus obtained passed the quality control and were processed for both types of profiling experiments as described below.

miRNA Expression Profiling

miRNAs were labeled and purified starting from 100 ng of total RNA of each sample and then hybridized on Mouse miRNA Microarrays v.21.0, 8 × 60 K (Agilent Technologies), according to the miRNA Complete Labeling and Hyb Kit Protocol (Version 3.1.1, August 2015). Microarrays were scanned at 3-μm resolution using a SureScan Microarray Scanner System (Agilent Technologies), and the Feature Extraction Software v. 11.5.1.1 (Agilent Technologies) was used for acquisition, data extraction, and quality control analysis. After the evaluation of quality control parameters for each scanned microarray image, the raw data of three replicates for wild-type and four replicates for knockout experimental conditions were analyzed using the Gene-Spring GX v.14.5 software (Agilent Technologies), by which fluorescence signal values were set at a threshold of 1, log2 transformed, and normalized using the 90th percentile shift method. The resulting data were baselined to the median of all samples and quality-filtered on flags to include any probe detected in 100% of biological replicates in at least one out of the two tested experimental conditions. Significantly deregulated miRNAs were identified using a moderate paired *t*-test and Benjamini–Hochberg multiple testing correction. MicroRNA profiling data were submitted to GEO (GSE151368).

Whole-Genome Transcription Profiling

Messenger RNA was labeled and purified starting from 100 ng of total RNA of each sample and then hybridized on SurePrint G3 Mouse Gene Expression v2 8 × 60 K Microarrays (Agilent Technologies), according to the One-Color Microarray-Based Gene Expression Analysis—Low Input Quick Amp Labeling kit protocol (Version 6.9.1, December 2015). Microarrays were scanned at 3-μm resolution using a SureScan Microarray Scanner System (Agilent Technologies), and the Feature Extraction Software v. 11.5.1.1 (Agilent Technologies) was used for acquisition, data extraction, and quality control analysis. The raw data of all samples were analyzed using the Gene-Spring GX v.14.5 software (Agilent Technologies). Fluorescence signal values were set at a threshold of 1, log2 transformed, normalized to the 75th percentile, baselined to the median of all samples, and quality-filtered on flags to include any probe detected in 100% of biological replicates in at least one out of the two tested experimental conditions. Differentially expressed genes (DEGs) were identified by a moderate *t*-test and Westfall–Young multiple testing correction. Data were submitted to GEO (GSE151367).

To perform gene set-focused expression analysis, we selected two gene lists from the Gene Ontology (GO) Resource knowledgebase (http://geneontology.org/) and its AmiGO tool (http://amigo.geneontology.org/amigo) using "glutathione" and "homocysteine" as keywords and filtering for *M. musculus*. The two selected gene lists made up of glutathione-related genes (n.86) and homocysteine-related (n.17) genes are, respectively, available in **Supplementary Tables 1**, **2**. To identify DEGs between knockout and wild-type animals in each gene set-focused list, a moderate *t*-test was applied without correction.

Functional Annotation and Enrichment

To functionally annotate DEGs and their products, we used the DAVID Bioinformatics Resources v. 6.8 public database (https://david.ncifcrf.gov/), together with the MetaCore software from Clarivate Analytics (https://portal.genego.com/); Mouse Genome Database (http://www.informatics.jax.org/); and the UniProt knowledgebase (http://www.uniprot.org).

Integrated Analysis of miRNA and mRNA Expression

To identify miRNA targets, we used the list of significant differentially expressed miRNAs as input queries for the DIANA-TarBase v7.0 tool (http://www.microrna.gr/tarbase), which contains high-quality manually curated experimentally validated miRNA–gene interactions inferred from published data, using the species *M. musculus* and 30 validation methods as filters. To annotate deregulated miRNAs with no validated gene targets in the DIANA-TarBase, we used three tools for miRNA target prediction, miRWalk v2.0 (http://zmf.umm.uni-heidelberg.de/apps/zmf/mirwalk2/), miRDB (http://www.mirdb.org/), and RNA22 v2.0 (https://cm.jefferson.edu/rna22/), selecting target genes if present in two out of three of them (**Supplementary Table 3**). The list of validated target genes for each miRNA was used as input for the target network analysis described below.

Network Analysis

To better clarify the interactions between gene targets of deregulated miRNAs at protein level, an extended protein–protein interaction (PPI) network was built using the STRING

database v.10.0, visualized with the Cytoscape v.3.4.0 software, and analyzed through its Network Analyzer plug-in. A network was built using 2,914 miRNA target genes as seed molecules (the entire workflow of analysis, setting, and filter values are summarized in **Supplementary Figure 2**). A network topology analysis was also performed on the base of topological parameters to identify hub nodes or proteins having a higher degree of connectivity reflecting their biological relevance. The final PPI network was visualized on the base of node degree and edge betweenness parameters. The relative importance of the network proteins was determined based on the node centrality measure and setting the topological parameter "node degree" to ≥10. Likewise, values of edge betweenness (≥50) were mapped with the edge size: high values of this parameter correspond to a large edge size, where edge indicates interactions.

qPCR Quantitative Analysis of Cx26, Cx30, and p53 Transcript Levels

RNA was extracted from whole cochleae freshly isolated from Cx30$^{+/+}$ and Cx30$^{-/-}$ mice at P5 using an RNeasy kit (Cat. No. 74104, Qiagen, Milan, Italy). cDNA was obtained by reverse transcription of mRNA with Oligo(dT)12–18 (Cat. No. 18418012, Thermo Fisher Scientific, Milan, Italy) and OmniScript Reverse Transcriptase (Cat. No. 205111, Qiagen) for 1 h at 37°C. qPCR was performed on cDNA to amplify Cx26, Cx30, and p53 and normalized to GAPDH expression (Pfaffl, 2001). Amplification was carried out using SYBR Green (Cat. No. 4367659, Applied Biosystems) on the ABI 7700 sequence detection system equipped with the ABI Prism 7700 SDS software using the following amplification cycles:

50°C, 2 min;
95°C, 10 min;
95°C, 15 sec; and
60°C, 1 min (40 cycles).

Primers used are listed as follows:
Cx26f: 5′-TCACAGAGCTGTGCTATTTG-3′
Cx26r: 5′-ACTGGTCTTTTGGACTTTCC-3′
Cx30f: 5′-GGCCGAGTTGTGTTACCTGCT-3′
Cx30r: 5′-TCTCTTTCAGGGCATGGTTGG-3′
p53f: 5′-GTATTTCACCCTCAAGATCC-3′
p53r: 5′-TGGGCATCCTTTAACTCTA-3′
GAPDHf: 5′-ATGTGTCCGTCGTGGATCTGAC-3′
GAPDHr: 5′-AGACAACCTGGTCCTCAGTGTAG-3′.

Immunohistochemistry and Confocal Imaging

Animals were terminally anesthetized (ketamine, 70 mg/g for males and 100 mg/g for females, and medetomidine 1 mg/g), their cochleae were quickly removed, and samples were fixed with 4% paraformaldehyde in phosphate-buffered saline (PBS) at 4°C and pH 7.5. For all immunofluorescence analyses, control experiments were performed by omitting the primary antibody during the processing of tissues, randomly selected across experimental groups. Staining was absent in these control cochlear samples, indicating neither autofluorescence nor lack of antibody specificity (data not shown). Tissues from all groups were always processed together to limit variability related to antibody penetration, incubation time, post-sectioning age, and condition of tissue.

Cx26 and Cx30 Immunofluorescence Analysis

To evaluate Cx30 and Cx26 expression in cochlear structures, cochleae from Cx30$^{+/+}$ and Cx30$^{-/-}$ mice were decalcified for 3 days in EDTA (0.3 M). Specimens were included in 3% agarose dissolved in PBS and cut into 100-μm thickness steps using a vibratome (VT 1000 S, Leica). Tissue slices were permeabilized with 0.1% Triton X-100, dissolved in 2% bovine serum albumin solution. Cx26 and Cx30 were immunolabeled by overnight incubation at 4°C with mouse monoclonal selective antibodies (Cx26, 10 μg/ml, Thermo Fisher, Cat. No. 335800; Cx30, 10 μg/ml, Thermo Fisher, Cat. No. MA5-35021) followed by incubation with a goat anti-mouse IgG secondary antibody (10 μg/ml, Alexa Fluor® 488, Thermo Fisher, Cat. No. A11029), applied at room temperature (22–25°C). F-actin was stained by incubation with Alexa Fluor 568 phalloidin (1 U/ml, Thermo Fisher, Cat. No. A12380), and nuclei were stained with 4′,6-diamidino-2-phenylindole (DAPI, Thermo Fisher, Cat. No. D1306) (1:200).

DHE Staining on Cochlear Tissue Cryosections

Cochleae of Cx30$^{+/+}$ and Cx30$^{-/-}$ terminally anesthetized mice were quickly removed and fixed with 4% paraformaldehyde in PBS at 4°C. Next, cochleae were decalcified in 10% EDTA (changed daily), incubated for 48 h in sucrose (30%), embedded in OCT and cryosectioned (6 μm). To evaluate the superoxide amount, cochlear slices were incubated with 1 mM DHE (Cat. No. D23107, Thermo Fisher) in PBS for 30 min at 37°C, embedded in antifade medium, and sealed with coverslips. DHE was imaged using an ultrafast tunable mode-locked titanium: sapphire laser (Chameleon; Coherent, 792 nm, 140 fs, 80 MHz) coupled to a multiphoton microscope (Nikon) equipped with a 20× Plan Apo objective (0.75 NA, Nikon).

p53 and Sirt1 Immunofluorescence

Cochlear cryosections (6 μm) were first treated with a blocking solution (1% BSA, 0.5% Triton X-100, and 10% normal goat serum in PBS 0.1 M) and then incubated overnight at 4°C with a solution containing primary antibodies against p53 (Cat. No. #2524, Cell Signaling Tech, Boston, MA USA, diluted 1:100 in PBS) and Sirt1 (Cat. No. #9475, Cell Signaling Tech, diluted 1:100 in PBS). Next, specimens were incubated at room temperature for 2 h in labeled-conjugated donkey anti-rabbit and/or anti-mouse secondary antibody (Alexa Fluor 488 or 546, IgG, Thermo Fisher, diluted 1:400 in PBS) and counterstained with DAPI (Cat. No. D1306, Thermo Fisher; 1:500). Images were obtained with the confocal laser scanning system (Nikon Ti-E, Confocal Head A1 MP, Japan) equipped with an Ar/ArKr laser (for 488-nm excitation), an HeNe laser (for 543-nm excitation), and a 20× Plan Apo objective (0.75 NA, Nikon). DAPI was imaged by two-photon excitation (740 nm, <140 fs, 90 MHz as detailed above).

Extravasation Assay

$Cx30^{+/+}$ and $Cx30^{-/-}$ mice at 3 months of age (3m) were anesthetized by intraperitoneal injections of ketamine (35 mg/kg) and medetomidine (1 mg/kg). Next, 30 μl of dye-containing solution (Texas Red™ dextran 70,000 MV, Invitrogen, Cat. No. 1987295, dissolved in PBS at a concentration of 2.5 mg/ml) was injected via the tail vein. After 3 min, injected animals were euthanized by cervical dislocation, cochleae were dissected in ice-cold PBS, and the spiral ligament and *SV* were microdissected from the rest of the cochleae. *SV* strips were detached from the spiral ligament and mounted onto glass slides with a mounting medium (FluorSave™ Reagent, Cat. No. 345789-20M, Merck). Images were obtained with a confocal laser scanning system mentioned above equipped with a 20× dry objective (20X PL Fluotar 0.5, NA, Leica). The fluorescent intensity of each area of interest was quantified with ImageJ (version 2.0.0-rc-69/1.53c), and statistics were computed using MATLAB R2019b on $n = 3$ mice for each genotype.

Western Immunoblots

Total proteins were extracted from cochleae of $Cx30^{+/+}$ and $Cx30^{-/-}$ animals ($n = 8$ animals per group). Cochleae were dissected, collected on ice, stored at −80°C, and homogenized by using ice-cold RIPA buffer [Pierce: 50 mM Tris, 150 mM NaCl, 1 mM EDTA, 1% DOC, 1% Triton X-100, 0.1% SDS, 1× protease, phosphatase-1, and phosphatase-2 inhibitor cocktails (Merck)]. The lysate was sonicated three times at 10 Hz (Hielscher, Ultrasound Technology UP50H/UP100H), centrifuged (13,000 rpm, 15 min, 4°C), and a 5-μl aliquot of the supernatant was assayed to determine the protein concentration (microBCA kit, Pierce). Reducing sample buffer was added to the supernatant, and samples were heated to 95°C for 5 min. Protein lysates (70 μg) were loaded onto Tris-glycine polyacrylamide gels for electrophoretic separation. Colorburst™ electrophoresis markers (Bio-Rad or Amersham) were used as molecular mass standards. Proteins were then transferred onto nitrocellulose membranes at 100 V for 2 h at 4°C in transfer buffer containing 25 mM Tris, 192 mM glycine, 0.1% SDS, and 20% methanol. Membranes were incubated for 1 h with blocking buffer (5% skim milk in TBST) and then incubated overnight at 4°C with the following primary antibodies: anti-Cx26 (mouse monoclonal, Cat. No. 335800, Thermo Fisher Scientific); anti-Cx30 (mouse monoclonal, Cat. No. MA5-35021, Thermo Fisher Scientific); anti-p53 (mouse monoclonal, Cat. No. #2524, Cell Signaling Tech); and anti-Sirt1 (rabbit polyclonal, Cat. No. 07-131, Merck Millipore). After three 10-min rinses in TBST, membranes were incubated for 1 h at RT horseradish peroxidase (HRP)-conjugated mouse or rabbit secondary antibodies (Cat. No. #7076 and Cat. No. #7074, respectively, Cell Signaling, 1:2,500). Equal protein loading among individual lanes was confirmed by reprobing the membranes with an anti-GAPDH (1:10,000, Cat. No. ab8245, Abcam) or anti-tubulin mouse monoclonal antibody (1:10,000, Cat. No. T6074, Sigma). Membranes were then washed and bands visualized with an enhanced chemiluminescence detection kit (Cat. No. K-12045-D50, Advansta). Protein expression was evaluated and documented by using UVITEC (Cambridge Alliance).

Statistical Analysis

For normally distributed data, statistical comparisons of means data were made by Student's two-tailed *t*-test using a worksheet (Microsoft Office Excel 2017, Version 1.30), whereas ANOVA and *post-hoc* comparison by Tukey's test were used to analyze the differences among group means using Statistica (version 6.0, StatSoft Inc.). The same software was also used to perform the Mann–Whitney *U*-test on data that did not require the assumption of normal distribution. Mean values are quoted ± standard error of the mean (s.e.m.) where $p < 0.05$ indicate statistical significance.

Study Approval

All experimental protocols involving the use of animals (*M. musculus*) were approved by the Ethical Committee of Padua University (Comitato Etico di Ateneo per la Sperimentazione Animale, C.E.A.S.A., Project no. 58/2013, protocol no. 104230) and the Italian Ministry of Health (DGSAF 0001276-P-19/01/2016 and 68/2016-PR). Experimental procedures were also agreed upon, reviewed, and approved by local animal welfare oversight bodies and were performed with the approval and direct supervision of the CNR-IBBC/Infrafrontier—Animal Welfare and Ethical Review Body (AWERB), in accordance with general guidelines regarding animal experimentation, approved by the Italian Ministry of Health, in compliance with the Legislative Decree 26/2014, transposing the 2010/63/EU Directive on protection of animals used in research. This work was also conducted based on recommendations from both ARRIVE and PREPARE guidelines.

RESULTS

Identification of Early Degeneration Biomarkers and Deregulated Molecular Pathways at P5

Deregulation of miRNAs and the PPI Network of Their Targets

By comparing miRNA expression profiles at P5 across genotypes ($Cx30^{-/-}$ vs. $Cx30^{+/+}$, see Materials and Methods and **Supplementary Figures 1**, **2**), we identified a total of 16 deregulated miRNAs. As illustrated in **Figure 1** and reported in **Table 1**, 9 out of 16 overexpressed miRNAs (miR-18a-5p, miR-29b-3p, miR-29c-3p, miR-34a-5p, miR-34b-5p, miR-141-3p, miR-181a-1-3p, miR-301a-3p, miR-376a-3p) have been previously linked to apoptosis, oxidative stress, and degeneration of the cochlea during aging. Thus, our results suggest that connexin downregulation and/or dysfunction determines a miRNA-mediated response during early post-natal development, which may influence apoptosis, oxidative stress, and degeneration processes and which can be detected already at P5. This is much earlier than the time of cochlear sensory epithelium degeneration, which occurs from P18 onwards in this mouse model (Teubner et al., 2003).

The miR-29b/c controls glucocorticoid-induced apoptosis in human plasmacytoid dendritic cells (Hong et al., 2013). In mice, overexpression of miR-34a/c has been involved in drug-induced

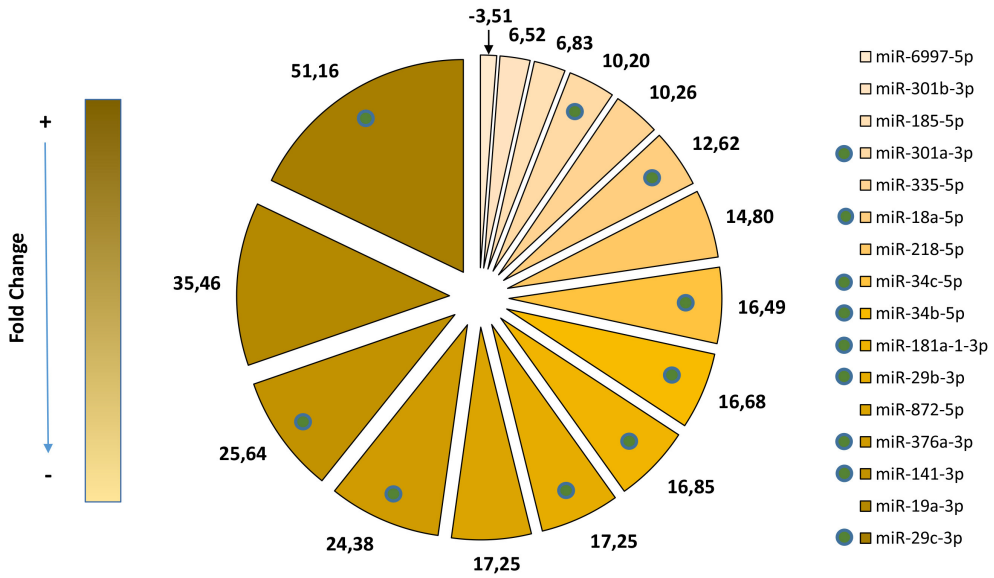

FIGURE 1 | Differentially expressed miRNAs. The pie chart shows significant changes in expression of 16 miRNAs, colored from light to dark gold according to their fold change expression value in *Cx30*$^{-/-}$ mice vs. controls with normal *Gjb6* alleles (*Cx30*$^{+/+}$). The fold change values are shown in clockwise order starting from the smallest one, indicating with an arrow the corresponding pie chart portion. Green tags highlight miRNAs already known as linked to apoptosis or deregulated in the degeneration of the cochlea during aging. Two of these upregulated miRNAs were already found as deregulated in sensorineural diseases of the ear, i.e., miR-18a and miR-376a, in mouse inner ear spatial expression patterns at P0, as previously reviewed (Ushakov et al., 2013; Mahmoodian sani et al., 2016). Moreover, the upregulation of miR-29b was detected in mouse vestibular sensory epithelium at P2 (Elkan-Miller et al., 2011) and in the degeneration of the mouse OC during aging (at 3m, 9m, and 16m compared to P21) (Zhang et al., 2013). Four other miRNAs, miR-29c, miR-34c, miR-141, miR-181a, and miR-301a, were previously described as dysregulated in mouse OC with age-related hearing loss (Zhang et al., 2013). In particular, miR-29b/c, miR-34a/c, and miR-181a are reported as pro-apoptotically deregulated in deafness due to aging (Khanna et al., 2011; Zhang et al., 2013).

hippocampal neurodegeneration (Cao et al., 2015), whereas overexpression of miR-34a and miR-34c has been implicated in drug-induced hearing loss (i.e., aminoglycoside-mediated ototoxicity) linked to dose-dependent apoptosis of inner ear cells (Yu et al., 2010). Finally, miR-141 and miR-181a were also found differentially expressed in reactive oxygen species (ROS)-damaged auditory cells (Wang et al., 2010).

To investigate the role of deregulated miRNAs, we searched the databases for their known validated targets (**Supplementary Table 3**). Five of these miRNAs (miR-34c, miR-29b, miR-29c, miR-141, and miR-181a) were previously linked to OC degeneration during age-related hearing loss (ARHL, also known as presbycusis) (Zhang et al., 2013) and share *Sirt1* as a common silencing gene target, which they are known to inhibit transcriptionally and/or post-transcriptionally in both humans and mice (**Table 1**). *Sirt1* encodes for the NAD^+-dependent deacetylase sirtuin 1 (Sirt1), a longevity modulator that exerts its deacetylation activity on several targets related to oxidative stress, inflammation, and apoptosis (Choi and Kemper, 2013). Like other sirtuins, it regulates antioxidant defense mechanisms involving antioxidant response elements (Singh et al., 2018). Sirt1 expression decreases with aging, whereas its increment has an antiaging role through multiple targets, including NFκB, p53, and PGC1α. Therefore, Sirt1 activation is thought to prolong life span and ameliorate age-related conditions (Chen et al., 2020b).

Two out of three of the miRNAs deregulated in our model (miRNA-34b-5p and miRNA-34c-5p) belong to the miRNA-34 family. Both are located in the same locus and coordinately expressed as a miRNA cluster in both humans and mice (Corney et al., 2007; He et al., 2007). Prior work implicated the miR-34a/Sirt1/p53 signaling pathway in cochlear cell apoptosis in an ARHL mouse model (Xiong et al., 2015). Although we did not detect differential expression of the miR-34a transcript in our model, the seed sequence of miR-34a and miR-34c is identical, suggesting that they can have the same targets (Rokavec et al., 2014). In fact, as shown in **Table 1**, *Sirt1* is a target also of miR-34c.

We also generated a PPI network downstream of miRNA deregulation, using network analysis of miRNA targets (**Figure 2A**; the entire lists of network nodes and their hubs are available in **Supplementary Tables 4**, **5**, respectively). In this scheme, the transcription factor p53 occupies a key position as a network hub downstream of miRNA deregulation (**Figure 2B**).

Taken together, these data suggested the involvement of a Sirt1–p53 axis downstream miRNA deregulation. Data regarding gene and protein expression of Sirt1 and p53 are provided in the sections below, related to the experimental validation of selected targets.

TABLE 1 | Deregulated miRNAs.

Up-regulated miRNAs in $Cx30^{KO}$ vs. $Cx30^{WT}$	miRNA detection	miRNAs:*Sirt1* known influence	
34c	Degeneration of the OC during ARHL (Zhang et al., 2013); kanamycin-induced apoptosis of inner ear cells (Yu et al., 2010); ketamine-induced neurotoxicity in neonatal mice hippocampus (Cao et al., 2015); development, cancerous, and non-cancerous diseases (Rokavec et al., 2014).	Cognitive decline in mouse hippocampus (Zovoilis et al., 2011); neuropathic pain in rat models with chronic constriction injury of the sciatic nerve (Mo et al., 2020).	Post-transcriptional inhibition (Zovoilis et al., 2011); transcriptional repression (Mo et al., 2020).
29b	Degeneration of the OC during ARHL (Zhang et al., 2013); mammalian inner ear (Elkan-Miller et al., 2011); glucocorticoid-induced apoptosis in human plasmacytoid dendritic cells (Hong et al., 2013).	Cochlear hair cell apoptosis in ARHL (Xue et al., 2016); oxidative stress in ovarian cancer (Hou et al., 2017); mouse embryonic stem cells in response to ROS (Xu et al., 2014).	Transcriptional repression (Xu et al., 2014; Xue et al., 2016; Hou et al., 2017).
29c	Degeneration of the OC during ARHL (Zhang et al., 2013); glucocorticoid-induced apoptosis in human plasmacytoid dendritic cells (Hong et al., 2013).	Tumor suppressor in hepatocellular carcinoma (Bae et al., 2014).	Post-transcriptional inhibition (Bae et al., 2014).
141	Degeneration of the OC during ARHL (Zhang et al., 2013); oxidative stress in auditory cells (Wang et al., 2010).	Autophagic response in hepatocytes (Yang et al., 2017); tumor suppressor in colorectal carcinoma cells (Sun et al., 2019).	Transcriptional repression (Yang et al., 2017; Sun et al., 2019).
181a	Degeneration of the OC during ARHL (Zhang et al., 2013); oxidative stress in auditory cells (Wang et al., 2010); Forskolin-treated basilar papillae (Frucht et al., 2010); hair cell regeneration in the avian auditory epithelium (Frucht et al., 2011); apoptosis and survival in the brain of calorie-restricted mice (Khanna et al., 2011).	Hepatic insulin signaling and glucose homeostasis (Zhou et al., 2012).	Post-transcriptional inhibition (Zhou et al., 2012).

The table lists deregulated miRNAs having Sirt1 as a common gene target and the model and pathologies in which their dysregulation has been detected. The mode of action of each miRNA on Sirt1 is also listed.

Transcriptional Profiling

We singled out 81 DEGs, among which 57 encode 56 proteins (**Supplementary Table 6**), and 15 correspond to non-coding RNAs (**Supplementary Table 7**). The co-regulated expression of *Cx30* and *Cx26*, previously described at the mRNA level (Ortolano et al., 2008), emerged also in these results, confirming that both connexins are downregulated in *Cx30*$^{-/-}$ mice. *Cx30*$^{-/-}$ and *Cx30*$^{+/+}$ mice expressed similar steady-state levels of *Sirt1* and *Tp53* mRNA, suggesting that deregulation of the Sirt1–p53 axis could be controlled post-transcriptionally by miRNAs, if present.

Our gene expression profiling also identified four downregulated transcripts, *Ang*, *Ang4*, and *Ang6*, which encode for three proteins belonging to the RNase A superfamily (Cho et al., 2005) (**Supplementary Table 6**). Of note, angiogenin (ANG) is a blood-vessel-inducing protein also expressed in vascular endothelial cells (Shimoyama, 2011). In addition, Ang4 is known to have an angiogenic role (Crabtree et al., 2007). Sirt1-dependent angiogenesis, where Sirt1 is a downstream mediator of angiogenic signals regulating vascular remodeling, was reported in mouse muscle vascularization. In particular, the loss of endothelial Sirt1 resulted in an early decline of skeletal muscle vascular density, while its overexpression had a protective effect (Das et al., 2018). Moreover, we report the overexpression of *Tnfrsf10b* (**Supplementary Table 6**), the tumor necrosis factor receptor superfamily member 10b gene encoding for a death receptor that is a known target of p53 (Speidel, 2010).

An increment of homocysteine caused by downregulation of *Bhmt*, a gene encoding betaine-homocysteine *S*-methyltransferase 1, was previously reported in P13 *Cx30*$^{-/-}$ mice and correlated to endothelial dysfunction in the *SV* (Cohen-Salmon et al., 2007). Here, we report downregulation of *Bhmt* already at P5 (**Supplementary Table 6**). This zinc metalloenzyme belongs to the trans-sulfuration pathway and catalyzes the subsequent conversion of methionine to homocysteine and cysteine, upstream of glutathione synthesis by glutathione synthetase (Gss) (Garrow, 1996). Importantly, we recently found deregulation of glutathione metabolism in *Cx26*$^{-/-}$ mice, in which reduced release of glutathione from connexin

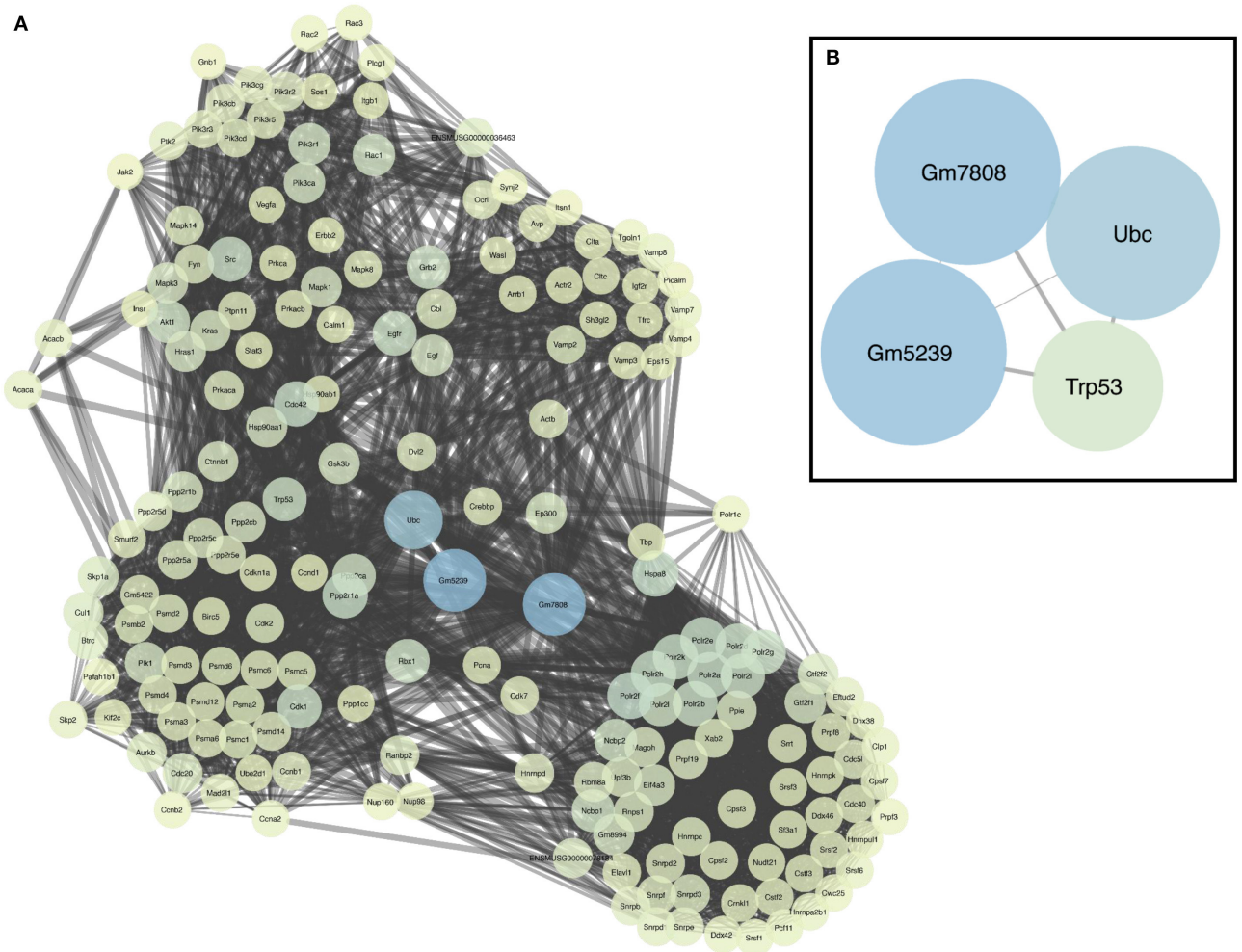

FIGURE 2 | PPI network. **(A)** Extended PPI network obtained using the miRNA target genes as input data (seeds). **(B)** A focus on network hubs among which is the transcription factor p53.

hemichannels has been also attributed to downregulation of *Gss* (Fetoni et al., 2018), a glutathione-related gene.

In light of these results, we performed a gene set-focused expression analysis on glutathione and homocysteine-related genes (**Supplementary Tables 1**, **2**). We detected the downregulation of *Gss* and the dysregulation of two other homocysteine-related genes, i.e., overexpression of C-1-tetrahydrofolate synthase (*Mthfd1*) and downregulation of *Bhmt*. The C-1-tetrahydrofolate synthase is a trifunctional protein involved in the tetrahydrofolate interconversion pathway, which interacts with the trans-sulfuration pathway at the homocysteine level (Ducker and Rabinowitz, 2017; Sbodio et al., 2019). Taken together, the results of this analysis support the involvement of homocysteine metabolism dysregulation in hearing loss.

MiR-34c-5p and Cx26

To identify possible transcriptional regulation between deregulated miRNAs and mRNAs, we compared the two lists of differentially expressed entities. This analysis yielded a matched list of differentially expressed miRNAs and their differentially expressed targets (**Supplementary Table 8**), among which only the downregulation of *Cx26* mediated by miR-34c-5p showed inverse deregulation between the overexpressed miRNA compared to its downregulated target gene. This direct regulation is reported in the DIANA-TarBase v7.0 tool, as inferred by crosslinking immunoprecipitation followed by RNA-seq in mouse regenerating liver (Schug et al., 2013). This miRNA–mRNA interaction was also predicted by the miRDB and RNA22 v2.0 databases.

The integration of miRNA profiling and transcriptional target analysis with gene expression profiling (taking into account pairs of experimentally validated miRNA/mRNA with an inverse correlation between their expression levels) suggested that transcriptional repression of *Cx26* could be modulated by miR-34c-5p action. In addition, other downregulated genes identified by our transcriptional profiling (**Supplementary Table 6**) have sequences complementary to

miR-34c/34b, including *Trpa1*, *Trpm1*, *Ang*, *Ang4*, and *Ang6*, which are predicted interactors of miR-34c/miR-34b in the RNA22 v2.0 database.

Oxidative Stress and Vascular Dysfunction

Immunofluorescence and Western Immunoblotting Analyses at P5

To confirm the absence of Cx30 and drastically reduced levels of Cx26 in the cochleae of *Cx30*$^{-/-}$ mice at P5, compared to age-matched *Cx30*$^{+/+}$ controls (wt), we performed immunofluorescence studies (**Supplementary Figure 3**) and Western blotting (**Supplementary Figure 4**) with selective antibodies. The same approach was used to study the expression levels of *Sirt1* and *Tp53* protein products. Our results confirmed the downregulation of Sirt1 protein in the cochlear duct of *Cx30*$^{-/-}$ mice, with the largest decrease observed in the *SV* and OC (**Figure 3** and **Supplementary Figure 5**), suggesting that its miRNA-mediated inhibition can be post-transcriptionally regulated in our model. In addition, the elevated levels of miR-34c highlighted by expression profiling correlated with a dramatic increment of p53 immunoreactivity in *Cx30*$^{-/-}$ cochleae (**Figure 4** and **Supplementary Figure 6**), suggesting that the Sirt1–p53 axis was regulated downstream the post-transcriptional inhibition of *Sirt1* by upregulated miRNAs.

Analysis of Oxidative Stress in the Cochlea at P5

As mentioned above, age-related cochlear hair cell apoptosis was linked to miR-34a/Sirt1/p53 action in a mouse model of ARHL (Xiong et al., 2015). It is well-known that oxidative stress is an aging hallmark and that an age-associated increase in oxidative stress reduces endothelial Sirt1 protein expression (Das et al., 2018). Therefore, we assayed oxidative stress levels in our model as previously done for conditional *Cx26*$^{-/-}$ mice (Fetoni et al., 2018). In *Cx30*$^{+/+}$ cochlear cryosections, superoxide levels (probed by DHE fluorescence, see Materials and Methods) were generally faint and slightly higher in spiral ganglion neurons (**Figure 5A**). In *Cx30*$^{-/-}$ cochleae, superoxide levels were markedly higher and particularly evident in spiral ganglion neurons, OC, and *SV* (**Figure 5B**). Together, these data signal the occurrence of early oxidative damage in *Cx30*$^{-/-}$ cochleae during post-natal development.

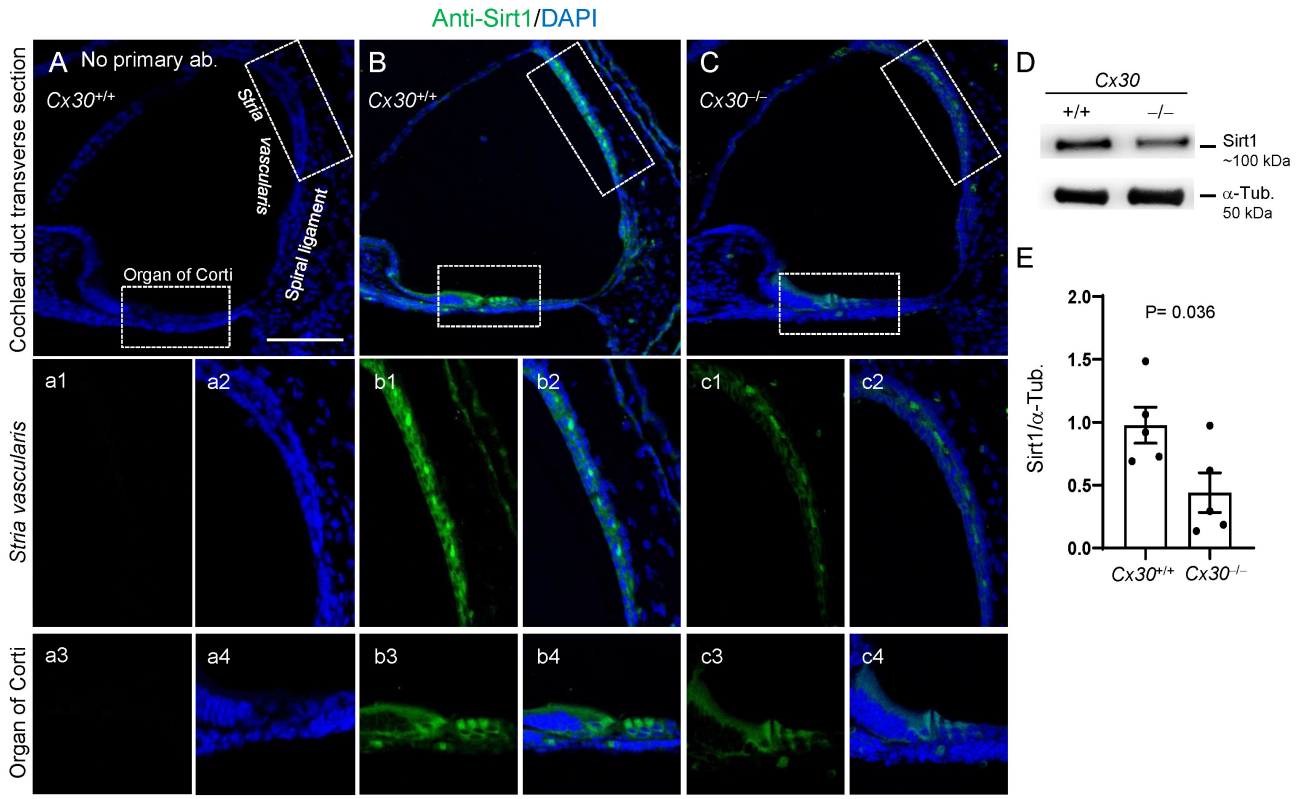

FIGURE 3 | Sirt1 expression in *Cx30*$^{+/+}$ and *Cx30*$^{-/-}$ cochleae at P5. **(A–C)** Representative images of immunofluorescence analysis with Sirt1-selective antibodies in the cochlear sensory epithelium and lateral wall of *Cx30*$^{+/+}$ and *Cx30*$^{-/-}$ **(B,C)** specimens. Images of negative control performed by omitting primary Sirt1 antibody are shown in **(A)**. **(a1–c4)** Higher magnification images of the OC and *SV* (dotted box in **A–C**) showing separately Sirt1 fluorescence **(a1,b1,c1,a3,b3,c3)** and merged Sirt1/DAPI nuclei staining **(a2,b2,c2,a4,b4,c4)**. Scale bar: 100 μm. **(D)** Representative western blot immunoreactive bands quantifying the expression of Sirt1 in *Cx30*$^{+/+}$ and *Cx30*$^{-/-}$ cochlear lysates. **(E)** Histograms indicate optical density values (mean ± SEM) of the western blots normalized to tubulin levels. Full-scan Western blot images are shown in **Supplementary Figure 5**.

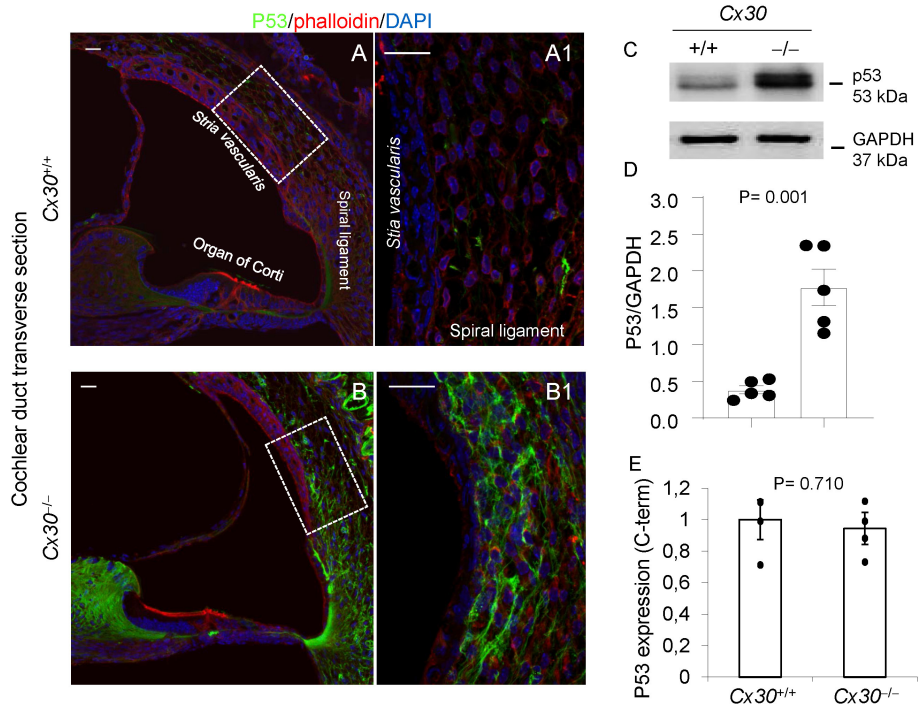

FIGURE 4 | p53 expression in *Cx30*$^{+/+}$ and *Cx30*$^{-/-}$ cochleae at P5. **(A,B)** p53 immunoreactivity in the cochlear duct **(A,B)** and lateral wall (shown magnified in **A1,B1**) of *Cx30*$^{+/+}$ and *Cx30*$^{-/-}$ cochleae at P5. Scale bars: 20 μm. **(C)** Representative western blot immunoreactive bands quantifying the expression of p53 in *Cx30*$^{+/+}$ and *Cx30*$^{-/-}$ cochleae (P5). **(D)** Optical density analysis (mean ± SEM) normalized to GAPDH. **(E)** qPCR quantitative analysis (mean ± SEM) of cochlear p53 transcript levels in *Cx30*$^{+/+}$ and *Cx30*$^{-/-}$ mice. Full-scan western blot images are shown in **Supplementary Figure 6**.

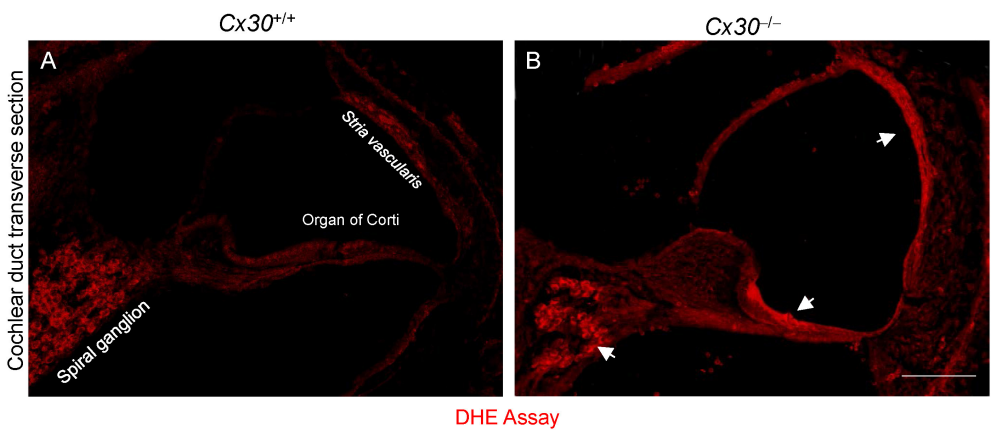

FIGURE 5 | Oxidative stress in *Cx30*$^{+/+}$ and *Cx30*$^{-/-}$ cochleae at P5. **(A,B)** Representative cochlear cryosections stained with DHE showing superoxide production (red fluorescence) in *Cx30*$^{+/+}$ and *Cx30*$^{-/-}$ cochleae. Arrows indicate increased fluorescence intensity in principal cochlear structures: *Stria vascularis*, organ of Corti, and spiral ganglion. Scale bar: 100 μm.

Analysis of Vascular Dysfunction in the *SV* at 3m

The *SV* has the highest aerobic metabolic rate of all cochlear structures, and its microvascular alterations contribute to age-related degeneration and progressive decline of auditory function. To examine the effects of oxidative damage on the *SV*, we injected Texas Red dextran via the caudal vein in *Cx30*$^{-/-}$ mice (at 3m) and age-matched *Cx30*$^{+/+}$ controls and examined dye fluorescence in *SV* whole mounts. **Figure 6** shows confocal images captured a few minutes after dye injection. There was no sign of dye extravasation in control littermates (**Figures 6A,A1**), whereas red fluorescence puncta were detected outside *SV* capillaries in *Cx30*$^{-/-}$ samples (see arrows in **Figures 6B,B1**), indicating disruption of the endothelial barrier in adulthood. Also, as shown in **Figure 6C**, quantitative

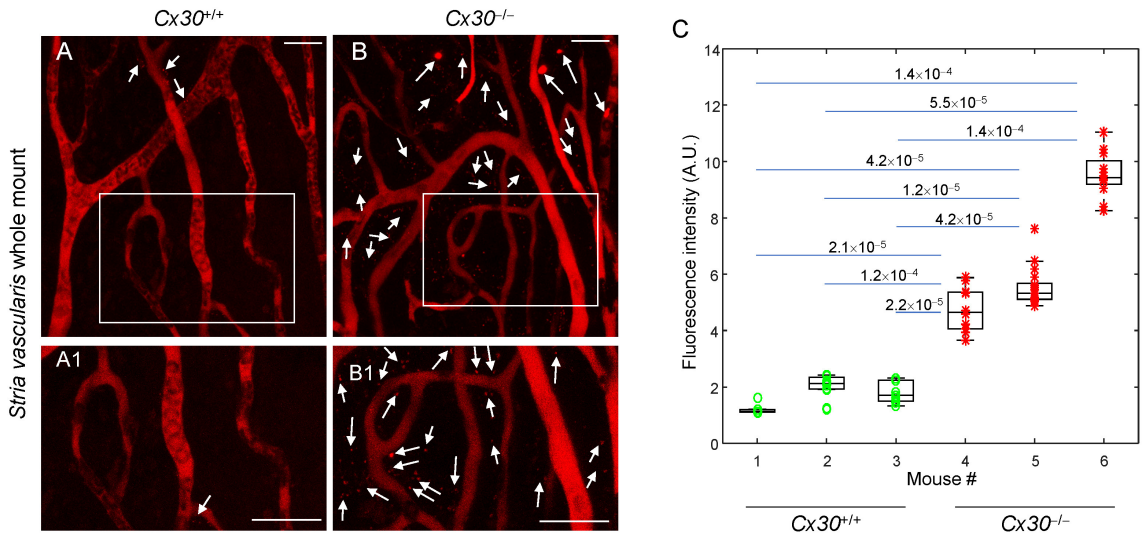

FIGURE 6 | Vascular dysfunction in *Cx30*$^{-/-}$ adult mice. **(A,B)** Representative images of freshly explanted *SV* from *Cx30*$^{+/+}$ and *Cx30*$^{-/-}$ mice (3 months of age) injected with a fluorescent Texas Red dextran (MW 70,000). Regions in the boxed areas are shown magnified in **(A1,B1)**. Arrows indicate dye lumps that leaked out of the vessels *Cx30*$^{-/-}$. Scale bars: 30 μm. **(C)** Quantification of Texas Red dextran fluorescence intensity (AU, arbitrary units) in *SV* of *Cx30*$^{+/+}$ and *Cx30*$^{-/-}$ samples. Data analysis was performed on $n = 3$ mice of each genotype; numbers above horizontal bars indicate *p*-values that were determined by the Mann–Whitney *U*-test, as implemented in the MATLAB function *ranksum*. Through-focus image sequences (z-stacks) corresponding to the images shown in this figure are provided as **Supplementary Video 1** (*Cx30*$^{+/+}$) and **Supplementary Video 2** (*Cx30*$^{-/-}$).

analysis of extravasation revealed a significant increase of Texas Red dextran fluorescence emission in the extravascular areas of *SV* of *Cx30*$^{-/-}$ mice compared to age-matched *Cx30*$^{+/+}$ controls.

DISCUSSION

In this work, we profiled miRNA and mRNA expression in the developing cochlea of a DFNB1 mouse model with global deletion of *Cx30* and severely reduced *Cx26* expression. Our results highlight an early oxidative stress that, later on, culminates in damage of the *SV*, a crucial vascularized epithelium of the cochlear lateral wall. The key protein Sirt1 (a NAD-dependent deacetylase protein) could mediate these processes, triggered by a lack of connexins. Our data suggest that Sirt1 downregulation could be potentially induced by miRNA negative influence and that it exerts its functions through p53, underlying hearing impairment.

The reduction of EP caused by *SV* dysfunction is responsible for strial ARHL in humans, as well as in mouse models of strial presbycusis (Keithley, 2019; Ohlemiller, 2019). EP reduction followed by mild hearing loss also affects a mouse model of digenic heterozygous deficiency of *Cx26* and *Cx30*, which causes impairment of heterotypic intercellular gap junctions coupling in the cochlear later wall (Mei et al., 2017). A recent study on *Cx30*$^{-/-}$ mice (the same strain used in this article) confirmed lack of EP at P18 preceded by failure of mitochondrial function and ATP synthesis, increment of oxidative stress, and dysregulated expression of proteins required for EP generation in *SV*. That study also showed a significant increment of the pro-apoptotic proteins Bax, Bad, and caspase-3 in the mouse cochlea, suggesting a Bax-mediated mitochondrial cell death from P18 onward (Chen et al., 2020a). Data supporting the importance of *SV* leakage underlying the pathogenic process of hearing impairment are emerging also in a mouse model with conditional deletion of *Cx43* (Zhang et al., 2020).

We identified five overexpressed miRNAs (miR-34c, miR-29b, miR-29c, miR-141, and miR-181a) linked to apoptosis, degeneration of cochlea during aging and oxidative stress, with *Sirt1* as a common gene target of transcriptional and/or post-transcriptional regulation (**Figure 1** and **Table 1**). Although *Sirt1* mRNA steady-state levels were not altered in *Cx30*$^{-/-}$ samples, our immunoassays confirmed an early Sirt1 expression decrement in the cochleae of *Cx30*$^{-/-}$ mice compared to controls. A miRNA-Sirt1 post-transcriptional influence has been validated in specific models (Zovoilis et al., 2011; Zhou et al., 2012; Bae et al., 2014). Therefore, *Sirt1* could be post-transcriptionally regulated by upregulated miRNAs, probably miR-34c, miR-29c, and miR-181a, in the cochleae of *Cx30*$^{-/-}$ mice at P5. In particular, miR-34c is our best candidate, as our data suggest it could regulate the expression of *Cx26* (transcriptionally) and of *Sirt1* (post-transcriptionally). Moreover, miR-34a, p53 acetylation, and apoptosis increase with aging in the cochleae of an ARHL mouse model, together with an age-related decrement of Sirt1, linking the miR-34a/Sirt1/p53 axis to age-related apoptosis of cochlear cells (Xiong et al., 2015). As previously mentioned, miR-34c shares an identical seed sequence with miR-34a, suggesting they can have the same targets

(Rokavec et al., 2014). In fact, miR-34c/Sirt1 post-transcriptional negative regulation was also described in a mouse model of cognitive decline (Zovoilis et al., 2011). Another work correlated age-dependent decrement of Sirt1 with increased miR-34a levels in the cochlea of an ARHL mouse model, accompanied by elevated hearing thresholds and loss of hair cells in the auditory cortex (Pang et al., 2016). The circulating plasma level of miRNA-34a was also significantly increased in human patients affected by ARHL (Pang et al., 2016). Moreover, increased levels of miR-34a were detected during endothelial cell senescence in an *in vitro* model and in older mice, and the effect of miR-34a upon senescence in endothelial cells was mediated by Sirt1 (Ito et al., 2010). It was also found that miR-34a levels increase during aging while Sirt1 levels decrease in murine aortas, and these changes correlated with an increased percentage of the senescence marker p16 and with miR-34a/Sirt1-mediated arterial dysfunctions (Badi et al., 2015). A correlation between SIRT1, Nrf2 and ROS production and their modulation by miR-34a in noise-induced hearing loss was reported also by Miguel et al. (2018).

Of note, Sirt1 was found abundantly expressed in the inner hair cells, strial marginal cells, and strial intermediate cells and moderately expressed in the outer hair cells and neurons of the auditory cortex and its significant reduction in a mouse model of ARHL correlated with elevated hearing thresholds and hair cell loss during aging (Xiong et al., 2014). In addition, the antiaging effect of a serotonin 5-HT3 receptor antagonist was assessed in a mouse model of induced senescence, resulting in the upregulation of *Sirt1* levels, increase of reduced glutathione concentration, decrease of inflammation biomarkers, increase of *Bcl-2*, and decrease of *Bax*, suggesting the regulation of oxidative stress, inflammation, and apoptosis was mediated by Sirt1 (Mirshafa et al., 2020).

The role of glutathione is particularly interesting, as we detected the downregulation of the potent antioxidant enzyme glutathione synthetase, *Gss* (**Supplementary Table 1**), also in a *Cx26* conditional knockout strain, accompanied by reduced release of glutathione through connexin hemichannels. In that work, we provided evidence of the consequent apoptosis and oxidative damage in the cochlear duct, offering a link between Cx26 monogenic hearing loss and ARHL (Fetoni et al., 2018). Moreover, the potent natural antioxidant and anti-inflammatory resveratrol is known to act on Sirt1, with positive antiaging effects on both brain (Sarubbo et al., 2017; Gomes et al., 2018) and vasculature (Kida and Goligorsky, 2016), also protecting vascular endothelial cells from atherosclerosis (a chronic inflammatory process associated with endothelial dysfunction and oxidative stress) (Wu et al., 2020). An oxidative stress increment in the *SV* was detected at P10 in *Cx30*$^{-/-}$ mice, along with a deregulated expression of genes encoding for catalases involved in oxidative stress in different cochlear regions and time points (Chen et al., 2020a), in accord with the results reported here.

Our immunoassay data indicate that Sirt1 decrement is significant in *SV* at P5 (**Figure 3**), and Sirt1 is also known as a regulator of angiogenic signaling during blood vessel growth, downregulating genes involved in vascularization (Potente et al., 2007). Here, we also reported the early downregulation of *Ang*, *Ang4*, and *Ang6* (**Supplementary Table 6**). Our data also showed the deregulation of the trans-sulfuration pathway (**Supplementary Tables 2**, **6**), which is part of the homocysteine metabolism upstream of glutathione synthesis (Ducker and Rabinowitz, 2017; Sbodio et al., 2019). Here, confirmed the downregulation of *Bhmt*, which was previously linked to elevated levels of homocysteine in the *SV* of *Cx30*$^{-/-}$ mice (Cohen-Salmon et al., 2007), and

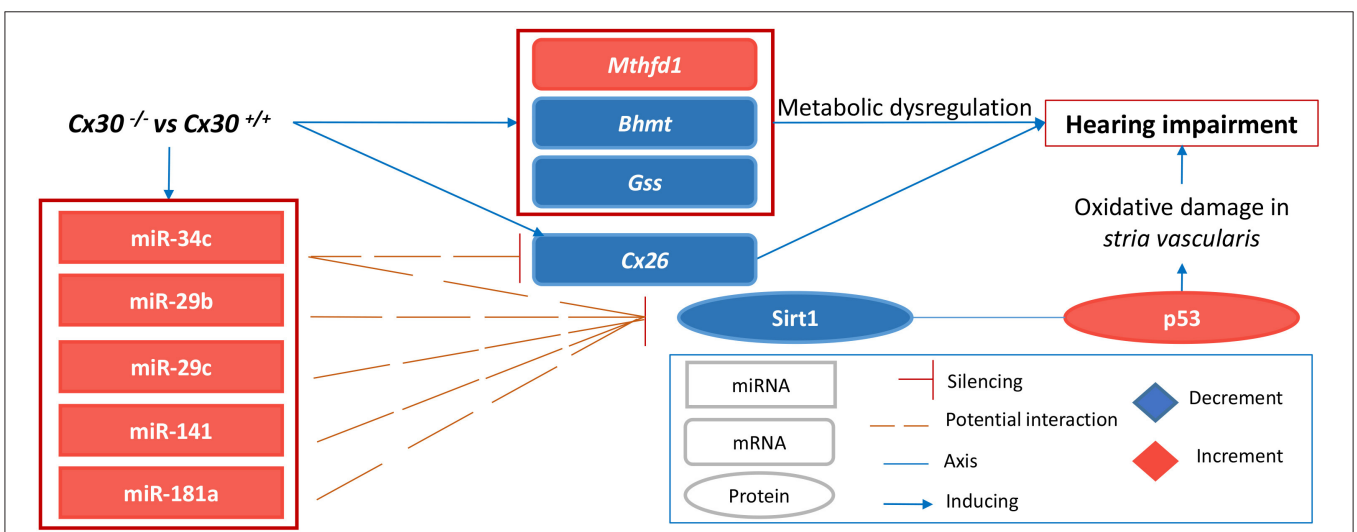

FIGURE 7 | Pathogenic mechanism proposed. The scheme describes our results in a mouse model of inherited digenic deafness at P5, highlighting an early involvement of a miRNA-mediated Sirt1–p53 axis as a nexus between oxidative stress in *SV*, metabolic dysregulation, and a hearing impairment occurring later in time with vascular dysfunction, which are all hallmarks of aging.

of *Mthfr*, another gene involved in homocysteine metabolism and hearing loss, even if its role in ARHL is controversial. Interestingly, hearing loss has been linked also to nutritional imbalance and oxidative stress, promoting the use of dietary supplementation as a nutritional therapy (Partearroyo et al., 2017).

As noted above, Sirt1 is known to prevent oxidative damage through different mechanisms, including the regulation of mitochondrial dysfunction and oxidative stress by p53 and NRF2 that in turn control the glutathione pathway (Singh et al., 2018). We detected an early (i) relevant increment of p53 immunoreactivity in the cochlear lateral wall (**Figure 4**), (ii) oxidative stress damage concentrated in the *SV* at P5 (**Figure 5**) and culminating in an extravasation phenomenon in strial explants of young adult *Cx30*$^{-/-}$ mice (**Figure 6**), and as previously discussed, (iii) the downregulation of *Gss* (**Supplementary Table 1**). Of note, our previous work on a Cx26 conditional knockout mouse model highlighted accelerated presbycusis caused by redox imbalance and dysregulation of Nrf2 antioxidant-response element-dependent genes related to glutathione metabolism (Fetoni et al., 2018). Moreover, Nrf2 seems to be also connected to the trans-sulfuration pathways (Sbodio et al., 2019).

In support of the involvement of p53, encoded by the *Trp53* gene, downstream of Sirt1, we also identified p53 as a hub of the PPI network built using all the deregulated miRNA targets of our model (**Figure 2** and **Supplementary Tables 4**, **5**). p53 is known to be a deacetylation target of Sirt1, exerting its pro-aging activity through the inhibition of DNA damage and stress-mediated cellular senescence. Consequently, inhibition of p53 by activation of SIRT1 has been proposed as a potential therapeutic strategy for aging-related diseases (Chen et al., 2020b). p53 regulates caspase-mediated apoptosis through two main mechanisms (and their cross talk): one is the extrinsic receptor-mediated pathway, acting via a transcription-dependent activity; the other is a transcription-independent activity that promotes mitochondrial outer membrane permeability (Speidel, 2010). As for the latter, wild-type p53 has been shown to localize at the endoplasmic reticulum (ER) and mitochondria-associated membranes (MAMs), where it interacts with sarco/ER Ca^{2+}-ATPase (SERCA) pumps, modulating ER–mitochondria cross talk and, in turn, Ca^{2+}-dependent apoptosis (Giorgi et al., 2015). In particular, activation and accumulation of p53 at the ER/MAMs render cells more prone to death, whereas absence of p53 leads to lower steady-state levels of reticular Ca^{2+}, reduced Ca^{2+} mobilization, and mitochondrial accumulation evoked by agonist stimulation (ATP) or oxidative stress (Giorgi et al., 2016). In support of the role of p53 in our model, we detected a relevant upregulation of the *Tnfrsf10b* at P5 (**Supplementary Table 6**), which encodes a death receptor also known as Dr5 that is a target of the transcription-dependent apoptotic activity of p53 (Speidel, 2010). Moreover, we already discussed a recent report suggesting that high levels of ROS may promote a Bax-mediated mitochondrial cell death from P18 onward in a *Cx30*$^{-/-}$ mouse model (Chen et al., 2020a). Taken together, these data suggest the involvement of the Sirt1–p53 axis as a nexus between (so far unrelated observations underlying) hearing impairment, vascular dysfunction, and aging in a mouse model of inherited digenic deafness (**Figure 7**).

In summary, our results suggest that inner ear connexin dysfunction in the *Cx30*$^{-/-}$ mouse model of DFNB1 promotes oxidative stress, apoptosis, and degeneration during early post-natal development, ensuing in cochlear vascular dysfunction later on in life, which are all hallmarks of ARHL. Our analysis links these pathological modifications to a Sirt1–p53 axis and its possible miRNA regulation. Strial atrophy is a known cause of sensorineural hearing loss (Pauler et al., 1988), and the crucial role of ion flow in *SV* and the production and regulation of cochlear endolymph and the endolymphatic potential is well-established. Moreover, studies in different rodent species showed age-related strial degeneration, coupled with an age-related reduction in the endolymphatic potential (Fetoni et al., 2011; Kujawa and Liberman, 2019). Furthermore, recent work on patients affected by severe ARHL (both sporadic and familial cases) demonstrated that ultrarare gene variants are causally linked to presbycusis where they were already known to cause dominant early-onset monogenic deafness (Boucher et al., 2020). In addition, Cx26 and Cx30 gap junctions are known to connect intermediate and basal cells of cochlear *SV* and play an important role in the generation of the endocochlear potential (Wangemann, 2006). It remains to be determined whether the observed vascular dysfunction is caused by reduction of Cx26 alone or in combination with Cx30. Further analysis is also necessary to extend our integrative analysis and directly validate miRNA/mRNA interaction. Although such studies pose important experimental challenges in the auditory organ, future experiments may help to identify novel therapeutic strategies.

DEDICATION

This work is dedicated to the memory of our colleague Barbara Maino.

DATA AVAILABILITY STATEMENT

The datasets presented in this study can be found in online repositories. The names of the repository/repositories and accession number(s) can be found at: https://www.ncbi.nlm.nih.gov/geo/query/acc.cgi?acc=GSE151368; https://www.ncbi.nlm.nih.gov/geo/query/acc.cgi?acc=GSE151367.

AUTHOR CONTRIBUTIONS

AF, SC, and FM: conceptualization. AS and MG: data curation. FP, VZ, and AS: formal analysis. MR, AF, SC, and FM: funding acquisition. GG, VZ, MG, and GC: investigation. GG, FP, AT-M, MR, AF, SC, and FM: methodology. AF, SC, and FM: resources. FS, MR, AF, SC, and FM: supervision. FP and VZ: validation.

FP, VZ, and AS: visualization. GG, FP, and FM: writing—original draft. AF, SC, and FM: writing—review and editing. All authors contributed to the article and approved the submitted version.

FUNDING

This work was supported by Fondazione Telethon (grant GGP13114) and Consiglio Nazionale delle Ricerche (CNR) Progetto di Interesse Invecchiamento (grant DSB.AD009.001.004/INVECCHIAMENTO-IBCN) to FM, CNR Project DSB.AD009.001.018/Invecchiamento-ISN and Italian Ministry of Education, Universities and Research grant PON R&C CTN01_00177_817708 to SC, fellowships granted to GG and AS (PON R&C CTN01_00177_817708), the Italian Ministry of Education, Universities and Research grant PRIN 2017FTJ5ZE Sensory decay and aging to MR, and BRiC INAIL 2016-DiMEILA17, ONR Global (N62909-15-1-2002), and D1 intramural funds from Università Cattolica to AF. The funding source had no role in the study design; in the collection, analysis, and interpretation of data, in the writing of the report, and in the decision to submit the article for publication.

ACKNOWLEDGMENTS

We are grateful to Denis Cuccaro and Francesco Chiani for help with miRNA data interpretation and Giovanna Morello for her help in GEO data pre-submission.

SUPPLEMENTARY MATERIAL

The Supplementary Material for this article can be found online at: https://www.frontiersin.org/articles/10.3389/fcell.2020.616878/full#supplementary-material

Supplementary figures and tables can be found in Data Sheet 1 and 2 files, respectively.

REFERENCES

Badi, I., Burba, I., Ruggeri, C., Zeni, F., Bertolotti, M., Scopece, A., et al. (2015). MicroRNA-34a induces vascular smooth muscle cells senescence by SIRT1 downregulation and promotes the expression of age-associated pro-inflammatory secretory factors. *J. Gerontol. A Biol. Sci. Med. Sci.* 70, 1304–1311. doi: 10.1093/gerona/glu180

Bae, H. J., Noh, J. H., Kim, J. K., Eun, J. W., Jung, K. H., Kim, M. G., et al. (2014). MicroRNA-29c functions as a tumor suppressor by direct targeting oncogenic SIRT1 in hepatocellular carcinoma. *Oncogene* 33, 2557–2567. doi: 10.1038/onc.2013.216

Boucher, S., Wong Jun Tai, F., Delmaghani, S., Lelli, A., Singh-Estivalet, A., Dupont, T., et al. (2020). Ultrarare heterozygous pathogenic variants of genes causing dominant forms of early-onset deafness underlie severe presbycusis. *Proc. Natl. Acad. Sci. U.S.A.* 117, 31278–31289. doi: 10.1073/pnas.2010782117

Boulay, A., del Castillo, F. J., Giraudet, F., Hamard, G., Giaume, C., Petit, C., et al. (2013). Hearing is normal without connexin30. *J. Neurosci.* 33, 430–434. doi: 10.1523/JNEUROSCI.4240-12.2013

Cao, S., Tian, J., Chen, S., Zhang, X., and Zhang, Y. (2015). Role of miR-34c in ketamine-induced neurotoxicity in neonatal mice hippocampus. *Cell Biol. Int.* 39, 164–168. doi: 10.1002/cbin.10349

Ceriani, F., Pozzan, T., and Mammano, F. (2016). Critical role of ATP-induced ATP release for Ca^{2+} signaling in nonsensory cell networks of the developing cochlea. *Proc. Natl. Acad. Sci. U.S.A.* 113, E7194–E7201. doi: 10.1073/pnas.1616061113

Chen, B., Xu, H., Mi, Y., Jiang, W., Guo, D., Zhang, J., et al. (2020a). Mechanisms of hearing loss and cell death in the cochlea of connexin mutant mice. *Am. J. Physiol. Cell Physiol.* 319, C569–C578. doi: 10.1152/ajpcell.00483.2019

Chen, C., Zhou, M., Ge, Y., and Wang, X. (2020b). SIRT1 and aging related signaling pathways. *Mech. Ageing Dev.* 187:111215. doi: 10.1016/j.mad.2020.111215

Cho, S., Beintema, J. J., and Zhang, J. (2005). The ribonuclease A superfamily of mammals and birds: identifying new members and tracing evolutionary histories. *Genomics* 85, 208–220. doi: 10.1016/j.ygeno.2004.10.008

Choi, S. E., and Kemper, J. K. (2013). Regulation of SIRT1 by microRNAs. *Mol. Cells* 36, 385–392. doi: 10.1007/s10059-013-0297-1

Cohen-Salmon, M., Regnault, B., Cayet, N., Caille, D., Demuth, K., Hardelin, J. P., et al. (2007). Connexin30 deficiency causes instrastrial fluid-blood barrier disruption within the cochlear *Stria vascularis*. *Proc. Natl. Acad. Sci. U.S.A.* 104, 6229–6234. doi: 10.1073/pnas.0605108104

Corney, D. C., Flesken-Nikitin, A., Godwin, A. K., Wang, W., and Nikitin, A. Y. (2007). MicroRNA-34b and microRNA-34c are targets of p53 and cooperate in control of cell proliferation and adhesion-independent growth. *Cancer Res.* 67, 8433–8438. doi: 10.1158/0008-5472.CAN-07-1585

Crabtree, B., Holloway, D. E., Baker, M. D., Acharya, K. R., and Subramanian, V. (2007). Biological and structural features of murine angiogenin-4, an angiogenic protein. *Biochemistry* 46, 2431–2443. doi: 10.1021/bi062158n

Crispino, G., Di Pasquale, G., Scimemi, P., Rodriguez, L., Galindo Ramirez, F., De Siati, R. D., et al. (2011). BAAV mediated GJB2 gene transfer restores gap junction coupling in cochlear organotypic cultures from deaf Cx26Sox10Cre mice. *PLoS ONE* 6:e23279. doi: 10.1371/journal.pone.0023279

Das, A., Huang, G. X., Bonkowski, M. S., Longchamp, A., Li, C., Schultz, M. B., et al. (2018). Impairment of an endothelial NAD^+-H2S signaling network is a reversible cause of vascular aging. *Cell* 173, 74–89.e20. doi: 10.1016/j.cell.2018.02.008

Del Castillo, F. J., and Del Castillo, I. (2017). DFNB1 non-syndromic hearing impairment: diversity of mutations and associated phenotypes. *Front. Mol. Neurosci.* 10:428. doi: 10.3389/fnmol.2017.00428

Dolmetsch, R. E., Xu, K., and Lewis, R. S. (1998). Calcium oscillations increase the efficiency and specificity of gene expression. *Nature* 392, 933–936. doi: 10.1038/31960

Ducker, G. S., and Rabinowitz, J. D. (2017). One-carbon metabolism in health and disease. *Cell Metab.* 25, 27–42. doi: 10.1016/j.cmet.2016.08.009

Elkan-Miller, T., Ulitsky, I., Hertzano, R., Rudnicki, A., Dror, A. A., Lenz, D. R., et al. (2011). Integration of transcriptomics, proteomics, and microRNA analyses reveals novel microRNA regulation of targets in the mammalian inner ear. *PLoS ONE* 6:e18195. doi: 10.1371/journal.pone.0018195

Fetoni, A. R., Picciotti, P. M., Paludetti, G., and Troiani, D. (2011). Pathogenesis of presbycusis in animal models: a review. *Exp. Gerontol.* 46, 413–425. doi: 10.1016/j.exger.2010.12.003

Fetoni, A. R., Zorzi, V., Paciello, F., Ziraldo, G., Peres, C., Raspa, M., et al. (2018). Cx26 partial loss causes accelerated presbycusis by redox imbalance and dysregulation of Nfr2 pathway. *Redox Biol.* 19, 301–317. doi: 10.1016/j.redox.2018.08.002

Frucht, C. S., Santos-Sacchi, J., and Navaratnam, D. S. (2011). MicroRNA181a plays a key role in hair cell regeneration in the avian auditory epithelium. *Neurosci. Lett.* 493, 44–48. doi: 10.1016/j.neulet.2011.02.017

Frucht, C. S., Uduman, M., Duke, J. L., Kleinstein, S. H., Santos-Sacchi, J., and Navaratnam, D. S. (2010). Gene expression analysis of forskolin treated basilar papillae identifies microRNA181a as a mediator of proliferation. *PLoS ONE* 5:e11502. doi: 10.1371/journal.pone.0011502

Garrow, T. A. (1996). Purification, kinetic properties, and cDNA cloning of mammalian betaine- homocysteine methyltransferase. *J. Biol. Chem.* 271, 22831–22838. doi: 10.1074/jbc.271.37.22831

Giorgi, C., Bonora, M., Missiroli, S., Morganti, C., Morciano, G., Wieckowski, M. R., et al. (2016). Alterations in mitochondrial and endoplasmic reticulum signaling by p53 mutants. *Front. Oncol.* 6:42. doi: 10.3389/fonc.2016.00042

Giorgi, C., Bonora, M., Sorrentino, G., Missiroli, S., Poletti, F., Suski, J. M., et al. (2015). p53 at the endoplasmic reticulum regulates apoptosis in a Ca^{2+}-dependent manner. *Proc. Natl. Acad. Sci. U.S.A.* 112, 1779–1784. doi: 10.1073/pnas.1410723112

Gomes, B. A. Q., Silva, J. P. B., Romeiro, C. F. R., dos Santos, S. M., Rodrigues, C. A., Gonçalves, P. R., et al. (2018). Neuroprotective mechanisms of resveratrol in Alzheimer's disease: role of SIRT1. *Oxid. Med. Cell. Longev.* 2018:8152373. doi: 10.1155/2018/8152373

He, L., He, X., Lim, L. P., de Stanchina, E., Xuan, Z., Liang, Y., et al. (2007). A microRNA component of the p53 tumour suppressor network. *Nature* 447, 1130–1134. doi: 10.1038/nature05939

Hong, Y., Wu, J., Zhao, J., Wang, H., Liu, Y., Chen, T., et al. (2013). miR-29b and miR-29c are involved in toll-like receptor control of glucocorticoid-induced apoptosis in human plasmacytoid dendritic cells. *PLoS ONE* 8:e69926. doi: 10.1371/journal.pone.0069926

Hou, M., Zuo, X., Li, C., Zhang, Y., and Teng, Y. (2017). Mir-29b regulates oxidative stress by targeting SIRT1 in ovarian cancer cells. *Cell. Physiol. Biochem.* 43, 1767–1776. doi: 10.1159/000484063

Ito, T., Yagi, S., and Yamakuchi, M. (2010). MicroRNA-34a regulation of endothelial senescence. *Biochem. Biophys. Res. Commun.* 398, 735–740. doi: 10.1016/j.bbrc.2010.07.012

Keithley, E. M. (2019). Pathology and mechanisms of cochlear aging. *J. Neurosci. Res.* 98, 1674–1684. doi: 10.1002/jnr.24439

Khanna, A., Muthusamy, S., Liang, R., Sarojini, H., and Wang, E. (2011). Gain of survival signaling by down-regulation of three key miRNAs in brain of calorie-restricted mice. *Aging* 3, 223–236. doi: 10.18632/aging.100276

Kida, Y., and Goligorsky, M. S. (2016). Sirtuins, cell senescence, and vascular aging. *Can. J. Cardiol.* 32, 634–641. doi: 10.1016/j.cjca.2015.11.022

Kujawa, S. G., and Liberman, M. C. (2019). Translating animal models to human therapeutics in noise-induced and age-related hearing loss. *Hear. Res.* 377, 44–52. doi: 10.1016/j.heares.2019.03.003

Mahmoodian sani, M. R., Hashemzadeh-Chaleshtori, M., Saidijam, M., Jami, M. S., and Ghasemi-Dehkordi, P. (2016). MicroRNA-183 family in inner ear: hair cell development and deafness. *J. Audiol. Otol.* 20, 131–138. doi: 10.7874/jao.2016.20.3.131

Mammano, F. (2019). Inner ear connexin channels: roles in development and maintenance of cochlear function. *Cold Spring Harb. Perspect. Med.* 9:ea033233. doi: 10.1101/cshperspect.a033233

Mei, L., Chen, J., Zong, L., Zhu, Y., Liang, C., Jones, R. O., et al. (2017). A deafness mechanism of digenic Cx26 (GJB2) and Cx30 (GJB6) mutations: reduction of endocochlear potential by impairment of heterogeneous gap junctional function in the cochlear lateral wall. *Neurobiol. Dis.* 108, 195–203. doi: 10.1016/j.nbd.2017.08.002

Miguel, V., Cui, J. Y., Daimiel, L., Espinosa-Díez, C., Fernández-Hernando, C., Kavanagh, T. J., et al. (2018). The role of MicroRNAs in environmental risk factors, noise-induced hearing loss, and mental stress. *Antioxid. Redox Signal.* 28, 773–796. doi: 10.1089/ars.2017.7175

Mirshafa, A., Mohammadi, H., Shokrzadeh, M., Mohammadi, E., Talebpour Amiri, F., and Shaki, F. (2020). Tropisetron protects against brain aging via attenuating oxidative stress, apoptosis and inflammation: the role of SIRT1 signaling. *Life Sci.* 248:117452. doi: 10.1016/j.lfs.2020.117452

Mittal, R., Liu, G., Polineni, S. P., Bencie, N., Yan, D., and Liu, X. Z. (2019). Role of microRNAs in inner ear development and hearing loss. *Gene* 686, 49–55. doi: 10.1016/j.gene.2018.10.075

Mo, Y., Liu, B., Qiu, S., Wang, X., Zhong, L., Han, X., et al. (2020). Down-regulation of microRNA-34c-5p alleviates neuropathic pain via the SIRT1/STAT3 signaling pathway in rat models of chronic constriction injury of sciatic nerve. *J. Neurochem.* 154, 301–315. doi: 10.1111/jnc.14998

Ohlemiller, K. K. (2019). Mouse methods and models for studies in hearing. *J. Acoust. Soc. Am.* 146, 3668–3680. doi: 10.1121/1.5132550

Ortolano, S., Di Pasquale, G., Crispino, G., Anselmi, F., Mammano, F., and Chiorini, J. A. (2008). Coordinated control of connexin 26 and connexin 30 at the regulatory and functional level in the inner ear. *Proc. Natl. Acad. Sci. U.S.A.* 105, 18776–18781. doi: 10.1073/pnas.0800831105

Pang, J., Xiong, H., Yang, H., Ou, Y., Xu, Y., Huang, Q., et al. (2016). Circulating miR-34a levels correlate with age-related hearing loss in mice and humans. *Exp. Gerontol.* 76, 58–67. doi: 10.1016/j.exger.2016.01.009

Partearroyo, T., Vallecillo, N., Pajares, M. A., Varela-Moreiras, G., and Varela-Nieto, I. (2017). Cochlear homocysteine metabolism at the crossroad of nutrition and sensorineural hearing loss. *Front. Mol. Neurosci.* 10:107. doi: 10.3389/fnmol.2017.00107

Patel, M., and Hu, B. H. (2012). MicroRNAs in inner ear biology and pathogenesis. *Hear. Res.* 287, 6–14. doi: 10.1016/j.heares.2012.03.008

Pauler, M., Schuknecht, H. F., and White, J. A. (1988). Atrophy of the *Stria vascularis* as a cause of sensorineural hearing loss. *Laryngoscope* 98, 754–759. doi: 10.1288/00005537-198807000-00014

Pfaffl, M. W. (2001). A new mathematical model for relative quantification in real-time RT-PCR. *Nucleic Acids Res.* 29:e45. doi: 10.1093/nar/29.9.e45

Potente, M., Ghaeni, L., Baldessari, D., Mostoslavsky, R., Rossig, L., Dequiedt, F., et al. (2007). SIRT1 controls endothelial angiogenic functions during vascular growth. *Genes Dev.* 21, 2644–2658. doi: 10.1101/gad.435107

Rodriguez, L., Simeonato, E., Scimemi, P., Anselmi, F., Cali, B., Crispino, G., et al. (2012). Reduced phosphatidylinositol 4,5-bisphosphate synthesis impairs inner ear Ca^{2+} signaling and high-frequency hearing acquisition. *Proc. Natl. Acad. Sci. U.S.A.* 109, 14013–14018. doi: 10.1073/pnas.1211869109

Rokavec, M., Li, H., Jiang, L., and Hermeking, H. (2014). The p53/miR-34 axis in development and disease. *J. Mol. Cell Biol.* 6, 214–230. doi: 10.1093/jmcb/mju003

Sarubbo, F., Esteban, S., Miralles, A., and Moranta, D. (2017). Effects of resveratrol and other polyphenols on Sirt1: relevance to brain function during aging. *Curr. Neuropharmacol.* 16, 126–136. doi: 10.2174/1570159X15666170703113212

Sbodio, J. I., Snyder, S. H., and Paul, B. D. (2019). Regulators of the transsulfuration pathway. *Br. J. Pharmacol.* 176, 583–593. doi: 10.1111/bph.14446

Schug, J., McKenna, L. B., Walton, G., Hand, N., Mukherjee, S., Essuman, K., et al. (2013). Dynamic recruitment of microRNAs to their mRNA targets in the regenerating liver. *BMC Genomics* 14:264. doi: 10.1186/1471-2164-14-264

Schutz, M., Scimemi, P., Majumder, P., de Siati, R. D., Crispino, G., Rodriguez, L., et al. (2010). The human deafness-associated connexin 30 T5M mutation causes mild hearing loss and reduces biochemical coupling among cochlear non-sensory cells in knock-in mice. *Hum. Mol. Genet.* 19, 4759–4773. doi: 10.1093/hmg/ddq402

Shimoyama, S. (2011). Angiogenin, ribonuclease, RNase A family, 5. *Atlas Genet. Cytogenet. Oncol. Haematol.* 15, 244–251. doi: 10.4267/2042/44976

Singh, C. K., Chhabra, G., Ndiaye, M. A., Garcia-Peterson, L. M., Mac,K, N. J., and Ahmad, N. (2018). The role of sirtuins in antioxidant and redox signaling. *Antioxidants Redox Signal.* 28, 643–661. doi: 10.1089/ars.2017.7290

Speidel, D. (2010). Transcription-independent p53 apoptosis: an alternative route to death. *Trends Cell Biol.* 20, 14–24. doi: 10.1016/j.tcb.2009.10.002

Sun, X., Bai, Y., Yang, C., Hu, S., Hou, Z., and Wang, G. (2019). Long noncoding RNA SNHG15 enhances the development of colorectal carcinoma via functioning as a ceRNA through miR-141/SIRT1/Wnt/β-catenin axis. *Artif. Cells Nanomed. Biotechnol.* 47, 2536–2544. doi: 10.1080/21691401.2019.1621328

Teubner, B., Michel, V., Pesch, J., Lautermann, J., Cohen-Salmon, M., Söhl, G., et al. (2003). Connexin30 (Gjb6)-deficiency causes severe hearing impairment and lack of endocochlear potential. *Hum. Mol. Genet.* 12, 13–21. doi: 10.1093/hmg/ddg001

Ushakov, K., Rudnicki, A., and Avraham, K. B. (2013). MicroRNAs in sensorineural diseases of the ear. *Front. Mol. Neurosci.* 6:52. doi: 10.3389/fnmol.2013.00052

Wang, Z., Liu, Y., Han, N., Chen, X., Yu, W., Zhang, W., et al. (2010). Profiles of oxidative stress-related microRNA and mRNA expression in auditory cells. *Brain Res.* 1346, 14–25. doi: 10.1016/j.brainres.2010.05.059

Wangemann, P. (2006). Supporting sensory transduction: cochlear fluid homeostasis and the endocochlear potential. *J. Physiol.* 576, 11–21. doi: 10.1113/jphysiol.2006.112888

Wu, C. W., Nakamoto, Y., Hisatome, T., Yoshida, S., and Miyazaki, H. (2020). Resveratrol and its dimers ε-viniferin and δ-viniferin in red wine protect

vascular endothelial cells by a similar mechanism with different potency and efficacy. *Kaohsiung J. Med. Sci.* 36, 535–542. doi: 10.1002/kjm2.1219

Xiong, H., Dai, M., Ou, Y., Pang, J., Yang, H., Huang, Q., et al. (2014). SIRT1 expression in the cochlea and auditory cortex of a mouse model of age-related hearing loss. *Exp. Gerontol.* 51, 8–14. doi: 10.1016/j.exger.2013.12.006

Xiong, H., Pang, J., Yang, H., Dai, M., Liu, Y., Ou, Y., et al. (2015). Activation of miR-34a/SIRT1/p53 signaling contributes to cochlear hair cell apoptosis: implications for age-related hearing loss. *Neurobiol. Aging* 36, 1692–1701. doi: 10.1016/j.neurobiolaging.2014.12.034

Xu, Z., Zhang, L., Fei, X., Yi, X., Li, W., and Wang, Q. (2014). The miR-29b–Sirt1 axis regulates self-renewal of mouse embryonic stem cells in response to reactive oxygen species. *Cell. Signal.* 26, 1500–1505. doi: 10.1016/j.cellsig.2014.03.010

Xue, T., We i, L., Zha, D. J., Qiu, J. H., Chen, F. Q., Qiao, L., et al. (2016). miR-29b overexpression induces cochlear hair cell apoptosis through the regulation of SIRT1/PGC-1α signaling: Implications for age-related hearing loss. *Int. J. Mol. Med.* 38, 1387–1394. doi: 10.3892/ijmm.2016.2735

Yang, Y., Liu, Y., Xue, J., Yang, Z., Shi, Y., Shi, Y., et al. (2017). MicroRNA-141 targets Sirt1 and rduce HBV replication. *Cell. Physiol. Biochem.* 41, 310–322. doi: 10.1159/000456162

Yu, L., Tang, H., Hua Jiang, X., Ling Tsang, L., Wa Chung, Y., and Chang Chan, H. (2010). Involvement of calpain-I and microRNA34 in kanamycin-induced apoptosis of inner ear cells. *Cell Biol. Int.* 34, 1219–1225. doi: 10.1042/CBI20100515

Zhang, J., Wang, X., Hou, Z., Neng, L., Cai, J., Zhang, Y., et al. (2020). Suppression of connexin 43 leads to strial vascular hyper-permeability, decrease in endocochlear potential, and mild hearing loss. *Front. Physiol.* 11:974. doi: 10.3389/fphys.2020.00974

Zhang, Q., Liu, H., McGee, J., Walsh, E. J., Soukup, G. A., and He, D. Z. Z. (2013). Identifying microRNAs involved in degeneration of the organ of corti during age-related hearing loss. *PLoS ONE* 8:e62786. doi: 10.1371/journal.pone.0062786

Zhou, B., Li, C., Qi, W., Zhang, Y., Zhang, F., Wu, J. X., et al. (2012). Downregulation of miR-181a upregulates sirtuin-1 (SIRT1) and improves hepatic insulin sensitivity. *Diabetologia* 55, 2032–2043. doi: 10.1007/s00125-012-2539-8

Zhu, Y., Zong, L., Mei, L., and Zhao, H. B. (2015). Connexin26 gap junction mediates miRNA intercellular genetic communication in the cochlea and is required for inner ear development. *Sci. Rep.* 5:15647. doi: 10.1038/srep 15647

Zovoilis, A., Agbemenyah, H. Y., Agis-Balboa, R. C., Stilling, R. M., Edbauer, D., Rao, P., et al. (2011). microRNA-34c is a novel target to treat dementias. *EMBO J.* 30, 4299–4308. doi: 10.1038/emboj.2011.327

Conflict of Interest: The authors declare that the research was conducted in the absence of any commercial or financial relationships that could be construed as a potential conflict of interest.

SUPPLEMENTARY FIGURES

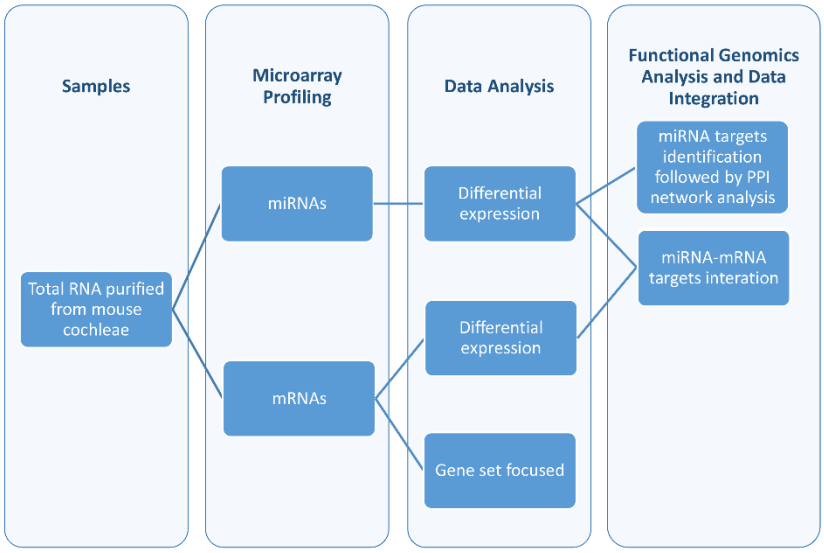

Figure S1. Data analysis flow chart. Methods used to analyse and integrate genomics data

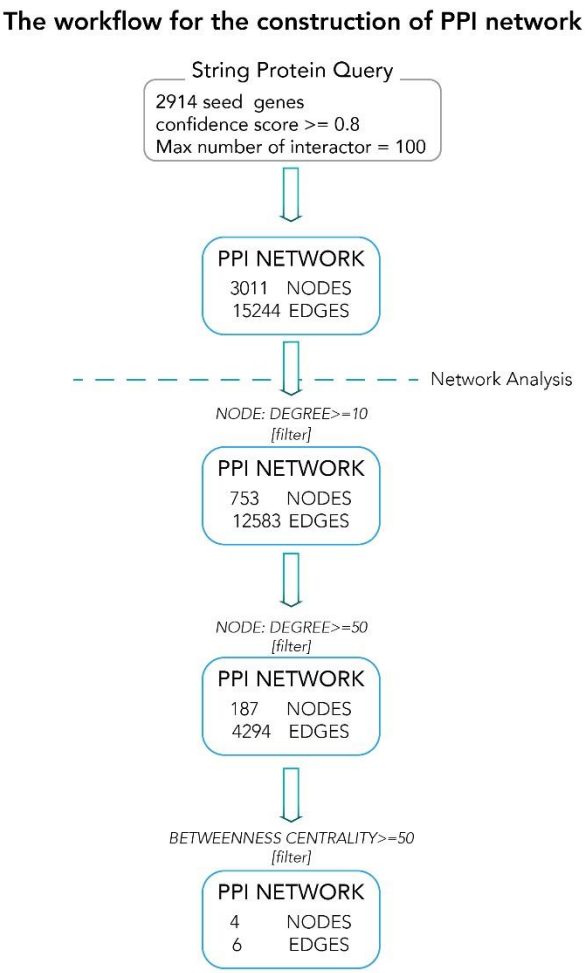

Figure S2. Workflow of PPI network construction and analysis. The workflow, setting and filter values used to obtain an extended PPI network, starting with 2914 target genes of the sixteen deregulated miRNAs as input data. Where nodes are proteins communicating in a biological network and edges indicate their interactions, while node degree and edge betweeness centrality represent topological parameters used to obtain hub nodes.

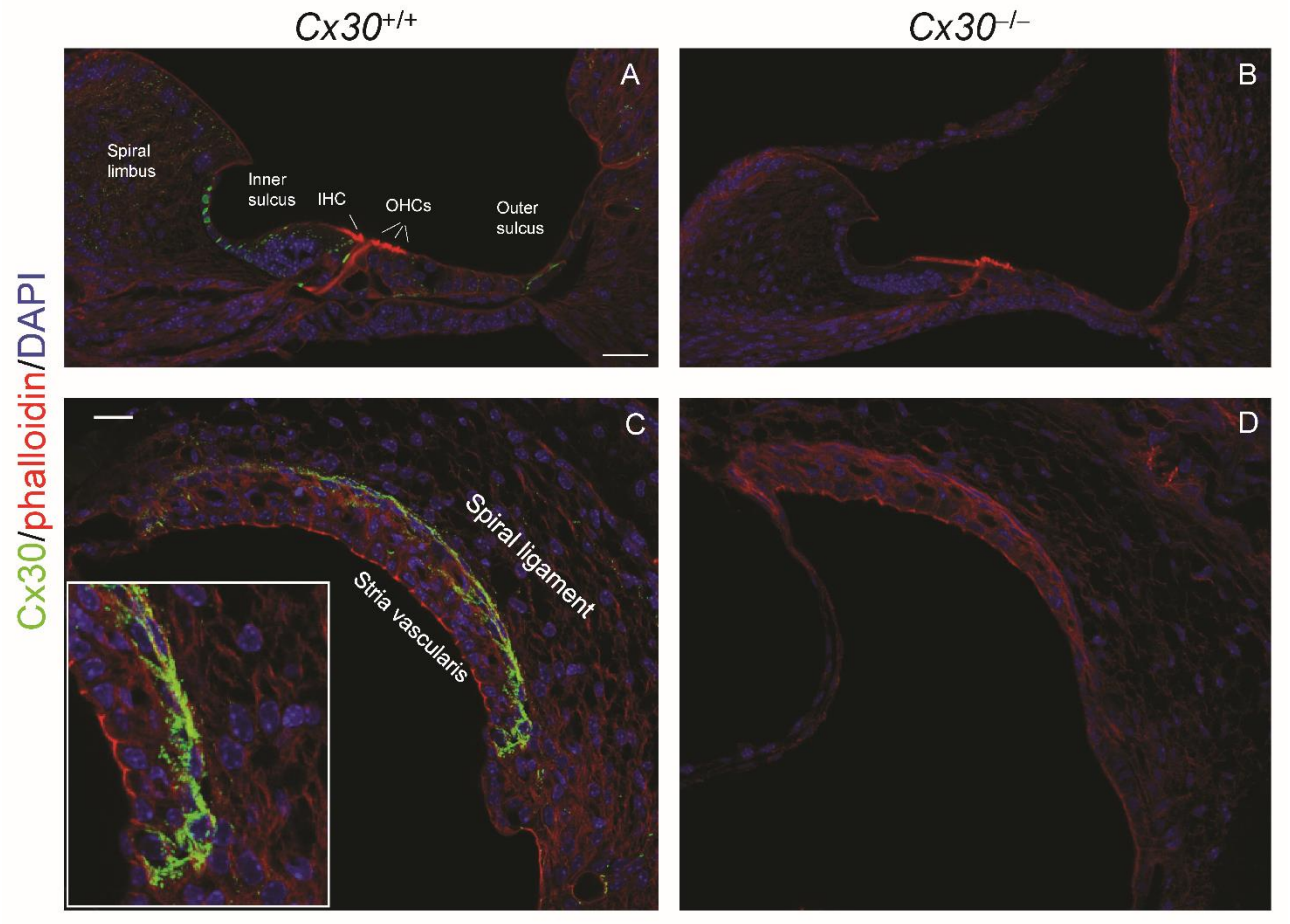

Figure S3. Connexin 30 localization in *Cx30*$^{+/+}$ and *Cx30*$^{-/-}$ cochleae at P5. A-D: Cx30 immunoreactivity in spiral limbus and sensory epithelium (A-B) lateral wall and stria vascularis (C-D) of *Cx30*$^{+/+}$ and *Cx30*$^{-/-}$ cochleae. Scale bar: 30 μm.

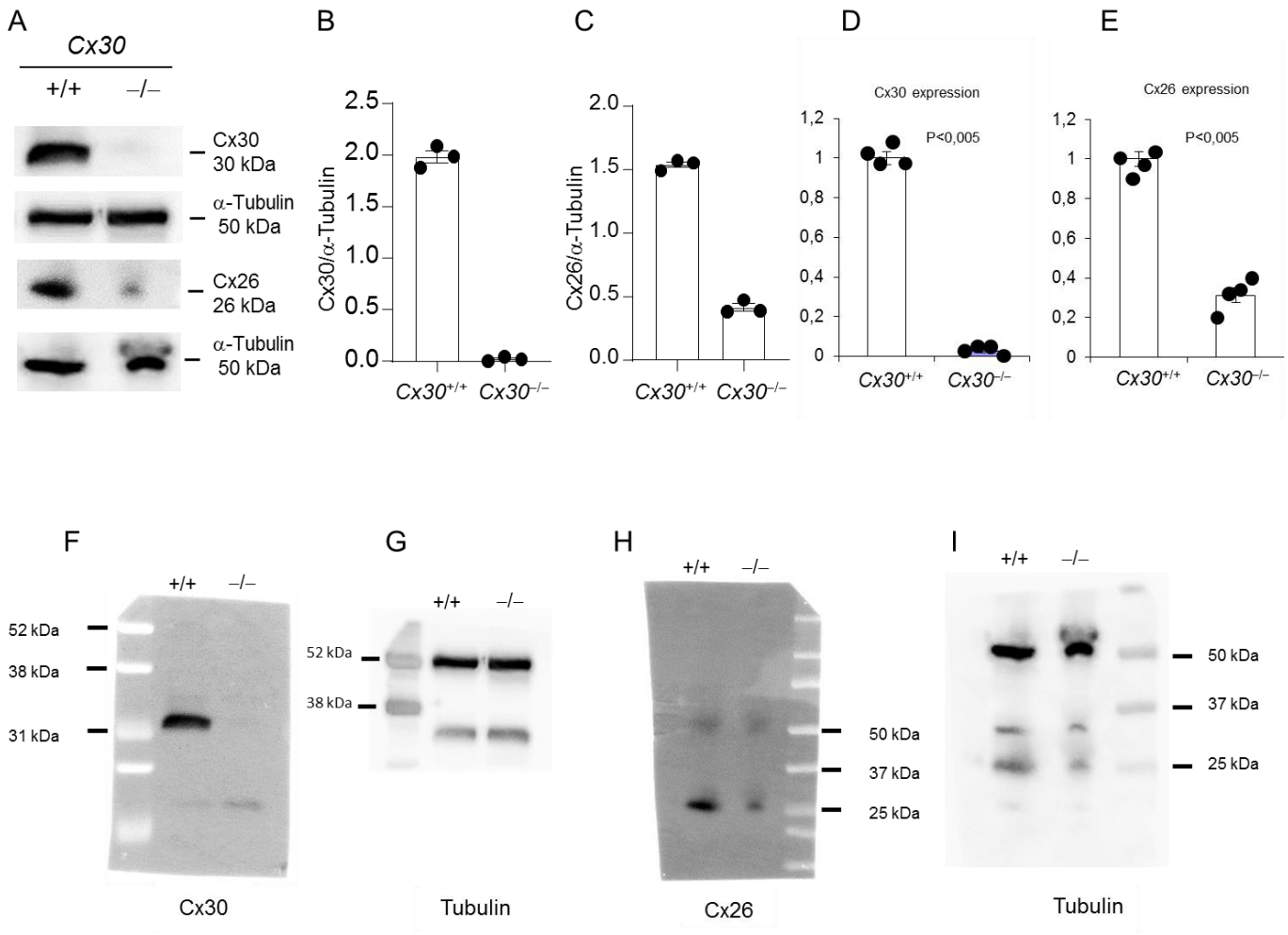

Figure S4. Cx30 and Cx26 expression in the cochlea of *Cx30*$^{+/+}$ and *Cx30*$^{-/-}$ mice at P5. A: Representative western blot immunoreactive bands showing the expression of Cx30 and Cx26 in *Cx30*$^{+/+}$ and *Cx30*$^{-/-}$ cochleae. B-C: Histograms (mean ± S.E.M.) represent optical density values normalized to α-tubulin levels. D-E: Histograms (mean ± S.E.M.) show qPCR quantitative analysis of cochlear Cx30 and Cx26 mRNA transcription in *Cx30*$^{+/+}$ and *Cx30*$^{-/-}$ cochleae. F-G: Uncropped western blot bands of western blot for Cx30 (F) and relative α-tubulin (G). H-I: Uncropped western blot bands of western blot for Cx26 (H) and relative α-tubulin (I).

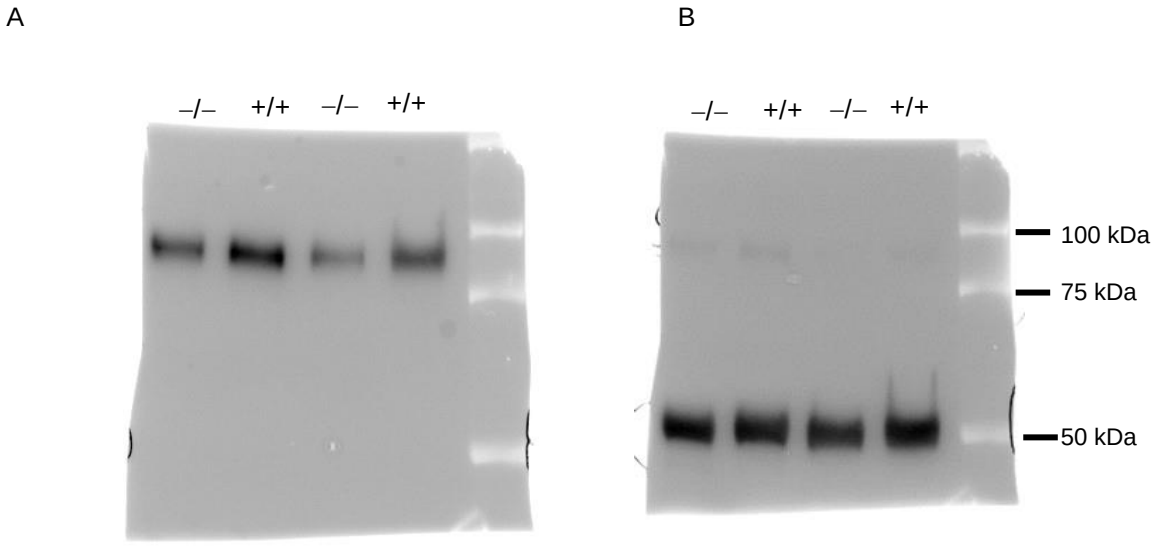

Figure S5. Uncropped western blot bands of western blot for Sirt1 (A) and α-tubulin (B), showed in Figure 3.

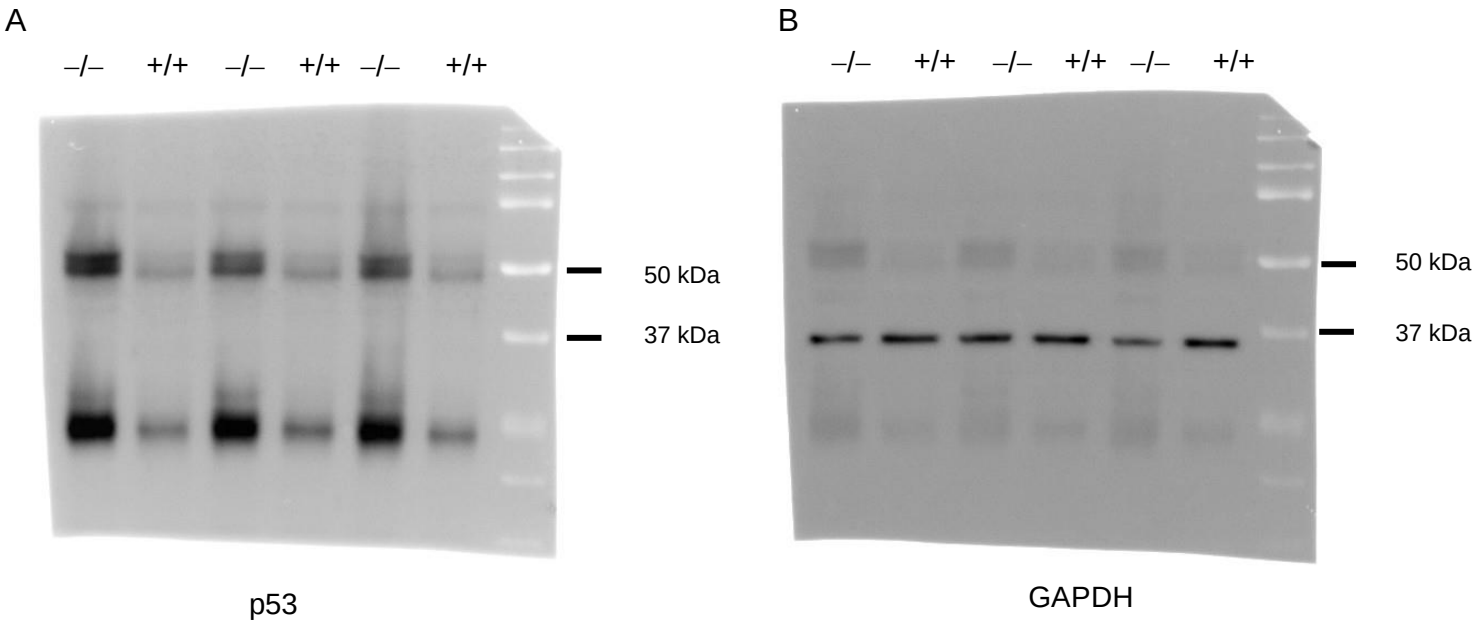

Figure S6. Uncropped western blot bands of western blot for p53 (A) and GAPDH (B), showed in Figure 4.

frontiers

Supplementary Tables

Supplementary Table S1. Gene set-focused analysis of glutathione-related genes. Lists of glutathione-related genes and their expression values by moderate T-test.

GLUTHATIONE GENE LIST

GeneSymbol	
Abcc1	*Gstp1*
Adh4	*Gstp2*
Adh5	*Gstp3*
Aldh5a1	*Gstt1*
Alox5ap	*Gstt2*
Chac1	*Gstt3*
Chac2	*Gstt4*
Cth	*Gstz1*
Ctns	*Hagh*
Eif2ak3	*Haghl*
Ethe1	*Hmgn5*
G6pdx	*Hpgds*
Gclc	*Idh1*
Gclm	*Lancl1*
Ggt1	*Ltc4s*
Ggt5	*Mgst1*
Ggt6	*Mgst2*
Ggt7	*Mgst3*
Glo1	*Mmachc*
Glrx	*Nat8*
Glrx3	*Nfe2l1*
Glrx5	*Nfe2l2*
Gm10639	*Oplah*
Gm20441	*Park7*
Gm6665	*Pdia3*
Gpx1	*Pnkd*
Gpx2	*Prdx6*
Gpx3	*Ptges*
Gpx4	*Slc22a8*
Gpx5	*Slc7a11*
Gpx6	*Slc9a3r1*
Gpx7	*Snca*
Gpx8	*Sod1*
Gsr	*Sod2*
Gss	*Txndc12*
Gsta1	*Txnrd3*
Gsta2	
Gsta3	
Gsta4	
Gstcd	
Gstk1	
Gstm1	
Gstm2	
Gstm3	
Gstm4	
Gstm5	
Gstm6	
Gstm7	
Gsto1	
Gsto2	

GLUTHATIONE MODERATED T-TEST

ProbeName	p ([WT] vs [KO])	Regulation	FC (abs)	FC	Log FC	[WT](raw)	[KO](raw)	[WT](normalized)	[KO](normalized)	GeneSymbol	Description	Sequence
A_66_P136921	0,008074958	down	1,5418512	-1,5418512	-0,6246635	270,19623	171,72308	0,30325353	-0,32140994	***Gss***	Mus musculus glutathione synthetase (Gss), transcript variant 1, mRNA [NM_008180]	AGAGGGTGGAGGTAACAACTTATAC GGGGAGGAAATGGTACAAGCTCTG GAGCAGCTGAA

Supplementary Table S2. Gene set-focused analysis of homocysteine-related genes. Lists of homocysteine-related genes and their expression values by moderate T-test.

HOMOCYSTEIN GENE LIST HOMOCYSTEIN MODERATED T-TEST

GeneSymbol	ProbeName	p ([WT] vs [KO])	Regulation	FC (abs)	FC	Log FC	[WT](raw)	[KO](raw)	[WT](normalized)	[KO](normalized)	GeneSymbol	Description	Sequence
Bhmt													
Bhmt2													
Blmh													
Cbs	A_55_P2740152	0,031401385	up	2,275023	2,275023	1,1858809	2468,771	5503,745	-0,9697015	0,21617937	***Mthfd1***	Mus musculus methylenetetrahydrofolate dehydrogenase (NADP+ dependent), methenyltetrahydrofolate cyclohydrolase, formyltetrahydrofolate synthase (Mthfd1), mRNA [NM_138745]	GAAGAGTACCACCACGATCGGG CTGGTGCAGGCCCTCGGCGCCC ACCTGCGACAGAACGT
Comt													
Cps1													
Cth													
Dpep1													
Herpud1	A_55_P2714597	0,002541643	down	2,057475	-2,057475	-1,040875	34,73928	16,545435	0,49040174	-0,5504731	***Bhmt***	Mus musculus betaine-homocysteine methyltransferase (Bhmt), mRNA [NM_016668]	ACAATGGACTGCTATTCTGTCTG CTTCTATTCCATTTCATTAATAAA AATGTGCTGGTTG
Mmut													
Mpst													
Mthfd1													
Mthfr													
Mtr													
Mtrr													
Nox4													
Tst													

Supplementary Table S3. Deregulated miRNAs in *Cx30*$^{-/-}$

Deregulated miRNAs	FC[a]	Validated targets[b]	Predicted targets[c]
mmu-miR-18a-5p	12.624649	403	-
mmu-miR-19a-3p	35.45887	749	-
mmu-miR-29b-3p	17.24806	813	-
mmu-miR-29c-3p	51.16448	273	-
mmu-miR-34b-5p	16.681662	4	-
mmu-miR-34c-5p	16.490164	227	-
mmu-miR-141-3p	25.640936	65	-
mmu-miR-181a-1-3p	16.851034	-	183
mmu-miR-185-5p	6.8337	116	-
mmu-miR-218-5p	14.799809	531	-
mmu-miR-301a-3p	10.196878	590	-
mmu-miR-301b-3p	6.519308	578	-
mmu-miR-335-5p	10.260769	504	-
mmu-miR-376a-3p	24.383179	-	118
mmu-miR-872-5p	17.254332	4	-
mmu-miR-6997-5p	-3.505543	-	28

[a,b] Fold change (FC) and number of miRNAs validated targets contained in DIANA-TarBase v7.0 are indicated.

[c] For the three deregulated miRNAs with no validated gene targets, three tools for miRNA targets prediction have been queried as described in Materials and Methods section.

Supplementary Table S4. PPI network nodes and their topological features

For all entries: Species = mus musculus; Node Type = protein; NameSpace = stringdb.; Is Single Node = false; Number of Directed Edges = 0; Partner of MultiEdge Node Pairs = 0; Selected = false; Self Loops = 0.

SUID	Database Identifier	Canonical Name	Name	Query Term	Description	Betweenness Centrality	Average Shortest Path Length	Clustering Coefficient	Closeness Centrality	Degree	Eccentricity	Neighborhood Connectivity	Number of Undirected Edges	Radiality	Stress	Topological Coefficient
11212	10090.ENSMUSP00000136791	J3QK04	Gm7808		predicted pseudogene 7808	0.07577783	236.340.534	0.10805452	0.42311828	270	7	4.564.814.815	270	0.89512267	10281420	0.04686668
14030	10090.ENSMUSP00000125548	O70435	Psma3	Psma3	proteasome (prosome, macropain) subunit, alpha type 3	8,62E+00	283.481.576	0.54828797	0.35275661	68	8	6.932.352.941	68	0.85886033	392322	
11733	10090.ENSMUSP00000059289	Q9Z0W3	Nup160	Nup160	nucleoporin 160	0.00212911	301.143.583	0.52308591	0.33206751	59	8	6.430.508.475	59	0.84527417	539728	0.1509509
12511	10090.ENSMUSP00000099475	Q68FD5	Cltc	Cltc	clathrin, heavy polypeptide (Hc)	0.00424863	281.639.136	0.56704261	0.35506429	57	7	580.877.193	57	0.86027759	580594	
13798	10090.ENSMUSP00000079124	O70201	Birc5	Birc5	baculoviral IAP repeat-containing 5	0.00480047	285.895.807	0.44243133	0.34977778	59	8	5.403.389.831	59	0.85700323	526110	
12009	10090.ENSMUSP00000029201	P42337	Pik3ca	Pik3ca	phosphatidylinositol 3-kinase, catalytic, alpha polypeptide	0.00724354	280.177.891	0.26035232	0.3569161	94	8	4.607.446.809	94	0.86140162	983148	
11498	10090.ENSMUSP00000028599	Q99LI7	Cstf3	Cstf3	cleavage stimulation factor, 3' pre-RNA, subunit 3	7,02E+00	323.697.586	0.89384921	0.30893032	64	8	7.778.125	64	0.82792493	263226	0.25585938
11499	10090.ENSMUSP00000033609	Q8BIQ5	Cstf2	Cstf2	cleavage stimulation factor, 3' pre-RNA subunit 2	0.00223153	316.899.619	0.84055944	0.31555734	66	8	76.0	66	0.83315414	427720	0.22749955
11244	10090.ENSMUSP00000032399	P32883	Kras	Kras	v-Ki-ras2 Kirsten rat sarcoma viral oncogene homolog	0.00873019	267.153.748	0.24593838	0.37431629	85	8	5.821.176.471	85	0.87142019	1550574	
12270	10090.ENSMUSP00000037268	Q8VDM6	Hnrnpul1	Hnrnpul1	heterogeneous nuclear ribonucleoprotein U-like 1	3.2E-7	324.396.442	0.99774011	0.30826479	60	8	81.85	60	0.82738735	48	0.27102649
13551	10090.ENSMUSP00000021447	Q61151	Ppp2r5e	Ppp2r5e	protein phosphatase 2, regulatory subunit B (B56), epsilon isoform	0.00222653	272.236.341	0.47167716	0.36732789	74	8	7.406.756.757	74	0.86751051	683436	0.10550936
12016	10090.ENSMUSP00000035037	Q8BTI9	Pik3cb	Pik3cb	phosphatidylinositol 3-kinase, catalytic, beta polypeptide	0.00190236	291.041.931	0.33654202	0.3435931	74	8	4.966.216.216	74	0.85304467	513772	
13809	10090.ENSMUSP00000051092	Q921L0	Picalm	Picalm	phosphatidylinositol binding clathrin assembly protein	0.00101318	289.834.816	0.71510204	0.34502411	50	7	62.98	50	0.85397322	242648	
12018	10090.ENSMUSP00000114180	Q9ET24	Ubc	Ubc	ubiquitin C	0.05482875	240.025.413	0.12827787	0.41662255	235	7	4.778.297.872	235	0.89228814	8010914	0.04982584
13043	10090.ENSMUSP00000030417	Q8BQ51	Cdc42	Cdc42	cell division cycle 42	0.03597249	258.005.083	0.16	0.38758926	126	8	4.927.777.778	126	0.87845763	3695196	
13047	10090.ENSMUSP00000097547	P39688	Fyn	Fyn	Fyn proto-oncogene	0.00895724	277.890.724	0.2436036	0.35985368	75	7	53.28	75	0.86316098	1113208	0.08689505
11263	10090.ENSMUSP00000021046	Q810A7	Ddx42	Ddx42	DEAD (Asp-Glu-Ala-Asp) box polypeptide 42	8,97E-02	324.205.845	0.94870439	0.30844601	62	8	7.975.806.452	62	0.82753397	65802	0.26322794
11265	10090.ENSMUSP00000133245	Q569Z5	Ddx46	Ddx46	DEAD (Asp-Glu-Ala-Asp) box polypeptide 46	8,97E-02	324.205.845	0.94870439	0.30844601	62	8	7.975.806.452	62	0.82753397	65802	0.26322794
12296	10090.ENSMUSP00000067786	Q62245	Sos1	Sos1	son of sevenless homolog 1 (Drosophila)	7,08E+00	304.193.139	0.38588235	0.32873851	51	8	5.531.372.549	51	0.84292835	95034	
12043	10090.ENSMUSP00000020085	P61080	Ube2d1	Ube2d1	ubiquitin-conjugating enzyme E2D 1	0.00125841	29.866.582	0.48838897	0.33482238	53	8	6.877.358.491	53	0.84718014	176542	
12047	10090.ENSMUSP00000018685	Q9DBF7	Cwc25	Cwc25	CWC25 spliceosome-associated protein homolog (S. cerevisiae)	3.2E-7	324.396.442	0.99774011	0.30826479	60	8	81.85	60	0.82738735	48	0.27102649
14097	10090.ENSMUSP00000001818	P63154	Crnkl1	Crnkl1	Crn, crooked neck-like 1 (Drosophila)	1,07E+00	323.697.586	0.92780338	0.30893032	63	8	7.885.714.286	63	0.82792493	69584	0.25854801
11539	10090.ENSMUSP00000047865	Q80X98	Dhx38	Dhx38	DEAH (Asp-Glu-Ala-His) box polypeptide 38	6,58E+00	323.697.586	0.92421915	0.30893032	63	8	7.903.174.603	63	0.82792493	183652	0.25912048
13588	10090.ENSMUSP00000070726	Q6PD03	Ppp2r5a	Ppp2r5a	protein phosphatase 2, regulatory subunit B (B56), alpha isoform	0.00289847	271.664.549	0.44019139	0.36810103	77	8	7.211.688.312	77	0.86795035	826016	0.10214856
11796	10090.ENSMUSP00000002198	Q8K4Z5	Sf3a1	Sf3a1	splicing factor 3a, subunit 1	9,78E-02	324.142.313	0.92524322	0.30850647	63	8	7.884.126.984	63	0.82758284	67270	0.26020221
12309	10090.ENSMUSP00000090059	Q62093	Srsf2	Srsf2	serine/arginine-rich splicing factor 2	4,99E+00	324.269.377	0.94606029	0.30838558	62	8	7.996.774.194	62	0.82748509	108198	0.26479385
12310	10090.ENSMUSP00000117045	P84104	Srsf3	Srsf3	serine/arginine-rich splicing factor 3	6.85E-6	32.433.291	0.97704918	0.30832517	61	8	812.295.082	61	0.82743622	1982	0.26897188
13592	10090.ENSMUSP00000002839	Q91V89	Ppp2r5d	Ppp2r5d	protein phosphatase 2, regulatory subunit B (B56), delta isoform	0.0028866	269.631.512	0.45684211	0.37087653	76	8	7.447.368.421	76	0.86951422	981326	
12570	10090.ENSMUSP00000003310	Q9ERU9	Ranbp2	Ranbp2	RAN binding protein 2	0.01282091	285.895.807	0.30935731	0.34977778	78	7	5.326.923.077	78	0.85700323	1371314	
12572	10090.ENSMUSP00000109635	Q9Z0R4	Itsn1	Itsn1	intersectin 1 (SH3 domain protein 1A)	0.00264335	278.907.243	0.57982583	0.35854214	53	8	679.245.283	53	0.86237904	361160	
12574	10090.ENSMUSP00000028475	Q99LI9	Clp1	Clp1	CLP1, cleavage and polyadenylation factor I subunit	2,05E+00	324.269.377	0.94764675	0.30838558	62	8	8.001.612.903	62	0.82748509	108362	0.26495407
12319	10090.ENSMUSP00000119065	Q3TWW8	Srsf6	Srsf6	serine/arginine-rich splicing factor 6	5,67E+00	323.761.118	0.91909882	0.3088697	63	8	789.047.619	63	0.82787606	212620	0.25955514
13088	10090.ENSMUSP00000028278	O35593	Psmd14	Psmd14	proteasome (prosome, macropain) 26S subunit, non-ATPase, 14	0.00140953	283.290.978	0.50422535	0.35299394	71	8	668.028.169	71	0.85900694	486442	0.11060069
12325	10090.ENSMUSP00000120595	Q6PDM2	Srsf1	Srsf1	serine/arginine-rich splicing factor 1	3,10E+00	324.269.377	0.94711793	0.30838558	62	8	7.998.387.097	62	0.82748509	163358	0.26484725
14119	10090.ENSMUSP00000053897	P70424	Erbb2	Erbb2	v-erb-b2 erythroblastic leukemia viral oncogene homolog 2	0.00347836	276.111.817	0.37330317	0.36217211	52	8	6.946.153.846	52	0.86452937	859710	0.10398434
11562	10090.ENSMUSP00000098066	Q6ZWM3	Actb	Actb	actin, beta	0.02938551	27.090.216	0.14475743	0.36913696	72	8	4.055.555.556	72	0.8685368	3243140	
12842	10090.ENSMUSP00000031695	Q91YD9	Wasl	Wasl	Wiskott-Aldrich syndrome-like (human)	0.00336312	277.001.271	0.49727768	0.36100917	58	8	6.324.137.931	58	0.86384518	472900	
13355	10090.ENSMUSP00000068487	Q62313	Tgoln1	Tgoln1	trans-golgi network protein	0.00393259	289.008.895	0.58333333	0.34601011	57	7	5.764.912.281	57	0.85460854	615888	0.10481659
11827	10090.ENSMUSP00000025705	Q62120	Jak2	Jak2	Janus kinase 2	0.00509007	301.016.518	0.28470588	0.33220768	51	7	4.503.921.569	51	0.84537191	618520	
13878	10090.ENSMUSP00000099790	P42567	Eps15	Eps15	epidermal growth factor receptor pathway substrate 15	0.00647547	287.865.311	0.61306122	0.34738468	50	8	62.22	50	0.85548822	488094	
12353	10090.ENSMUSP00000026416	P97377	Cdk2	Cdk2	cyclin-dependent kinase 2	0.00643497	275.349.428	0.32534247	0.3631749	73	8	5.947.945.205	73	0.86511582	744922	
11334	10090.ENSMUSP00000030940	P62874	Gnb1	Gnb1	guanine nucleotide binding protein (G protein), beta 1	0.00353346	299.491.741	0.29632653	0.33389902	50	8	43.92	50	0.84654481	608088	
11335	10090.ENSMUSP00000068148	Q9QXK7	Cpsf3	Cpsf3	cleavage and polyadenylation specificity factor 3	0.00167511	314.104.193	0.81908639	0.3183657	67	8	7.591.044.776	67	0.83530447	411886	0.21688699
12359	10090.ENSMUSP00000088845	Q03147	Cdk7	Cdk7	cyclin-dependent kinase 7	0.00422194	28.678.526	0.39464442	0.34869296	68	7	6.811.764.706	68	0.85631903	575048	
11336	10090.ENSMUSP00000047797	O35218	Cpsf2	Cpsf2	cleavage and polyadenylation specific factor 2	0.00167511	314.104.193	0.81908639	0.3183657	67	8	7.591.044.776	67	0.83530447	411886	0.21688699
11338	10090.ENSMUSP00000038958	Q8BTV2	Cpsf7	Cpsf7	cleavage and polyadenylation specific factor 7	6.85E-6	32.433.291	0.97704918	0.30832517	61	8	812.295.082	61	0.82743622	1982	0.26897188
13389	10090.ENSMUSP00000030014	Q3UYV9	Ncbp1	Ncbp1	nuclear cap binding protein subunit 1	0.00437275	284.879.288	0.47527473	0.35102587	105	7	6.654.285.714	105	0.85778516	888690	
13647	10090.ENSMUSP00000039269	Q96J62	Hnrnpk	Hnrnpk	heterogeneous nuclear ribonucleoprotein K	3.2E-7	324.396.442	0.99774011	0.30826479	60	8	81.85	60	0.82738735	48	0.27102649
12880	10090.ENSMUSP00000090177	A2A5Z6	Smurf2	Smurf2	SMAD specific E3 ubiquitin protein ligase 2	0.00293942	304.574.333	0.47371032	0.32832708	64	8	595.625	64	0.84263513	557410	0.14559138
13649	10090.ENSMUSP00000132735	Q60668	Hnrnpd	Hnrnpd	heterogeneous nuclear ribonucleoprotein D	0.0021145	300.190.597	0.67053999	0.33312169	77	7	8.619.480.519	77	0.84600723	509566	0.17808844
11858	10090.ENSMUSP00000023486	Q62351	Tfrc	Tfrc	transferrin receptor	0.00298658	289.390.089	0.66138763	0.34555434	52	7	60.75	52	0.85431532	289832	0.11085766
13652	10090.ENSMUSP00000107237	Q9Z204	Hnrnpc	Hnrnpc	heterogeneous nuclear ribonucleoprotein C	0.00414794	310.800.508	0.78028169	0.3217498	71	7	75.0	71	0.83784576	469254	0.20321386
11351	10090.ENSMUSP00000024599	Q07113	Igf2r	Igf2r	insulin-like growth factor 2 receptor	0.00168571	289.580.686	0.67043741	0.3453269	52	7	6.159.615.385	52	0.8541687	344664	
13400	10090.ENSMUSP00000071200	P08775	Polr2a	Polr2a	polymerase (RNA) II (DNA directed) polypeptide A	0.01129392	270.965.693	0.36292063	0.36905041	126	7	6.217.460.317	126	0.86848793	1919144	0.09102001
13403	10090.ENSMUSP00000025106	Q9D7M8	Polr2d	Polr2d	polymerase (RNA) II (DNA directed) polypeptide D	0.00558795	278.716.645	0.39269972	0.35878733	121	7	6.372.727.273	121	0.86252566	1434926	0.10278592
13408	10090.ENSMUSP00000021277	O70126	Aurkb	Aurkb	aurora kinase B	0.00533417	281.321.474	0.40538786	0.35546522	79	8	6.103.797.468	79	0.86052194	828892	
11879	10090.ENSMUSP00000062392	P20444	Prkca	Prkca	protein kinase C, alpha	0.01475222	289.771.283	0.15912519	0.34509976	52	8	45.5	52	0.85402209	2892732	0.08990861
11113	10090.ENSMUSP00000099587	P63087	Ppp1cc		protein phosphatase 1, catalytic subunit, gamma isoform	0.00676045	29.815.756	0.40808081	0.33539314	55	8	4.876.363.636	55	0.84757111	764734	
11114	10090.ENSMUSP00000019614	Q9DCD2	Xab2		XPA binding protein 2	0.00133821	294.218.551	0.76445967	0.33988339	73	8	8.446.575.342	73	0.85060111	427008	0.15847233
11115	10090.ENSMUSP00000021412	Q9QUM9	Psma6		proteasome (prosome, macropain) subunit, alpha type 6	8,62E+00	283.481.576	0.54828797	0.35275661	68	8	6.932.352.941	68	0.85886033	392322	
11116	10090.ENSMUSP00000115883	Q00731	Vegfa		vascular endothelial growth factor A	0.010165	276.683.609	0.28156749	0.36142365	53	8	5.011.320.755	53	0.86408953	1000710	0.07913798
11117	10090.ENSMUSP00000103483	B1AWD9	Clta		clathrin, light polypeptide (Lca)	0.00289664	281.575.604	0.60808081	0.3551444	55	7	5.998.181.818	55	0.86032646	488714	0.09753141
11118	10090.ENSMUSP00000021063	Q9D8W5	Psmd12		proteasome (prosome, macropain) 26S subunit, non-ATPase, 12	8,62E+00	283.481.576	0.54828797	0.35275661	68	8	6.932.352.941	68	0.85886033	392322	0.11477406
11375	10090.ENSMUSP00000018449	Q99PV0	Prpf8	Prpf8	pre-mRNA processing factor 8	0.00141218	323.506.989	0.84801865	0.30911233	66	8	7.537.878.788	66	0.82807155	444624	0.24714357
11119	10090.ENSMUSP00000017365	P14685	Psmd3		proteasome (prosome, macropain) 26S subunit, non-ATPase, 3	8,62E+00	283.481.576	0.54828797	0.35275661	68	8	6.932.352.941	68	0.85886033	392322	0.11477406
11120	10090.ENSMUSP00000022380	P62334	Psmc6		proteasome (prosome, macropain) 26S subunit, ATPase, 6	0.00183248	281.257.942	0.54433714	0.35554552	68	8	6.963.235.294	68	0.86057081	493568	0.11087954
13937	10090.ENSMUSP00000120152	P42227	Stat3	Stat3	signal transducer and activator of transcription 3	0.0072854	279.733.164	0.21945701	0.35748353	52	8	4.623.076.923	52	0.86174372	633556	0.07550905
11123	10090.ENSMUSP00000129767	P49722	Psma2		proteasome (prosome, macropain) subunit, alpha type 2	0.00188517	281.194.409	0.53282182	0.35562585	69	8	6.876.811.594	69	0.86061969	503910	
13171	10090.ENSMUSP00000020608	P63330	Ppp2ca	Ppp2ca	protein phosphatase 2 (formerly 2A), catalytic subunit, alpha isoform	0.01601033	257.814.485	0.27059787	0.3878758	111	8	6.463.963.964	111	0.87860424	3274218	
12916	10090.ENSMUSP00000034204	Q9CQF3	Nudt21	Nudt21	nudix (nucleoside diphosphate linked moiety X)-type motif 21	6.85E-6	32.433.291	0.97704918	0.30832517	61	8	812.295.082	61	0.82743622	1982	0.26897188
11125	10090.ENSMUSP00000030212	Q62420	Sh3gl2		SH3-domain GRB2-like 2	0.00186378	282.719.187	0.55974026	0.35370787	56	7	5.971.428.571	56	0.85944678	385056	0.10138249
11126	10090.ENSMUSP00000021306	O08810	Eftud2		elongation factor Tu GTP binding domain containing 2	0.00375683	321.029.225	0.73004695	0.31149812	72	8	7.168.055.556	72	0.82997752	534768	0.21920659
11127	10090.ENSMUSP00000135967	J3KMQ2	Gm5422		predicted pseudogene 5422	0.00492686	277.382.465	0.5054326	0.36051306	71	7	6.864.788.732	71	0.86355195	1038246	0.1054499
12151	10090.ENSMUSP00000113717	G3X9Z4	Pcf11	Pcf11	cleavage and polyadenylation factor subunit homolog (S. cerevisiae)	6.85E-6	32.433.291	0.97704918	0.30832517	61	8	812.295.082	61	0.82743622	1982	0.26897188
11128	10090.ENSMUSP00000007212	Q8VDM4	Psmd2		proteasome (prosome, macropain) 26S subunit, non-ATPase, 2	0.00492686	277.382.465	0.5054326	0.36051306	71	7	6.864.788.732	71	0.86355195	1038246	0.1054499
11129	10090.ENSMUSP00000021049	P62196	Psmc5		protease (prosome, macropain) 26S subunit, ATPase 5	0.00187496	28.252.859	0.52642796	0.35394648	69	8	6.879.710.145	69	0.85959339	470746	0.11168361
12410	10090.ENSMUSP00000087453	O88569	Hnrnpa2b1	Hnrnpa2b1	heterogeneous nuclear ribonucleoprotein A2/B1	0.00221933	31.797.967	0.93548387	0.31448551	62	8	7.972.580.645	62	0.83232333	233852	0.24232768

12666	10090.ENSMUSP00000041902	P22682	Cbl	Cbl	Casitas B-lineage lymphoma	0.00472283	273.506.989	0.37320574	0.36562137	77	8	6.323.376.623	77	0.86653309	908588					
11130	10090.ENSMUSP00000099404	Q62077	Plcg1		phospholipase C, gamma 1	0.01870028	302.795.426	0.24175084	0.33025598	55	8	4.294.545.455	55	0.84400352	5075970					
11131	10090.ENSMUSP00000064261	Q922S8	Kif2c		kinesin family member 2C	0.0037829	305.527.319	0.4996633	0.32730297	55	8	5.041.818.182	55	0.84190206	589986					
11388	10090.ENSMUSP00000028817	P17918	Pcna	Pcna	proliferating cell nuclear antigen	0.01449611	278.208.386	0.23611111	0.3594428	64	7	62.359.375	64	0.86291663	1133828					
11132	10090.ENSMUSP00000021091	P63005	Pafah1b1		platelet-activating factor acetylhydrolase, isoform 1b, subunit 1	0.00658241	297.141.042	0.45324675	0.33654052	56	8	4.991.071.429	56	0.84835304	806672					
11133	10090.ENSMUSP00000098897	Q9Z1B5	Mad2l1		MAD2 mitotic arrest deficient-like 1	0.00280869	287.102.922	0.51243781	0.34830715	67	8	6.714.925.373	67	0.85607468	464140					
11134	10090.ENSMUSP00000021595	P62192	Psmc1		protease (prosome, macropain) 26S subunit, ATPase 1	0.00113961	282.846.252	0.52898551	0.35354897	69	8	6.826.086.957	69	0.85934904	430908	0.11227117				
11135	10090.ENSMUSP00000022256	Q99JI4	Psmd6		proteasome (prosome, macropain) 26S subunit, non-ATPase, 6	9,74E+00	283.418.043	0.53623188	0.35283569	69	8	6.856.521.739	69	0.8589092	408594	0.11351857				
11136	10090.ENSMUSP00000087457	P09055	Itgb1		integrin beta 1 (fibronectin receptor beta)	0.00740168	313.087.675	0.25387755	0.31939935	50	8	37.52	50	0.8360864	1325574	0.10617564				
11137	10090.ENSMUSP00000024727	Q6A068	Cdc5l		cell division cycle 5-like (S. pombe)	0.00856412	321.346.887	0.71244131	0.31119019	72	8	6.941.666.667	72	0.82973316	1281404	0.22155662				
11138	10090.ENSMUSP00000084252	P52432	Polr1c		polymerase (RNA) I polypeptide C	0.00777053	299.047.014	0.39935065	0.33439558	56	8	5.330.357.143	56	0.84688691	602366	0.12542017				
11139	10090.ENSMUSP00000102857	O35226	Psmd4		proteasome (prosome, macropain) 26S subunit, non-ATPase, 4	0.00118691	283.354.511	0.52132505	0.3529148	70	8	6.784.285.714	70	0.85895807	473918	0.11232261				
11140	10090.ENSMUSP00000095866	Q8BWG8	Arrb1		arrestin, beta 1	0.00597543	279.987.294	0.51242938	0.35715907	60	7	58.55	60	0.86154824	697982					
11141	10090.ENSMUSP00000082053	Q60996	Ppp2r5c		protein phosphatase 2, regulatory subunit B (B56), gamma isoform	0.00369598	268.996.188	0.41835443	0.37175248	80	8	71.825	80	0.87000293	1151220					
11142	10090.ENSMUSP00000035551	P35455	Avp		arginine vasopressin	0.00651945	286.340.534	0.47749854	0.34923452	59	8	5.916.949.153	59	0.85666113	478100					
11143	10090.ENSMUSP00000020203	P62307	Snrpf		small nuclear ribonucleoprotein polypeptide F	6,29E-01	314.930.114	0.73898556	0.31753076	74	8	7.263.513.514	74	0.83466914	234504	0.20403128				
11144	10090.ENSMUSP00000128400	P62305	Snrpe		small nuclear ribonucleoprotein E	6,29E-01	314.930.114	0.73898556	0.31753076	74	8	7.263.513.514	74	0.83466914	234504	0.20403128				
11145	10090.ENSMUSP00000043123	Q99MR6	Srrt		serrate RNA effector molecule homolog (Arabidopsis)	5,04E+00	313.532.402	0.74126126	0.3189463	75	8	72.24	75	0.83574431	94358	0.21564179				
11146	10090.ENSMUSP00000018156	P60764	Rac3		RAS-related C3 botulinum substrate 3	0.00192355	306.226.175	0.23961039	0.32655602	56	8	3.741.071.429	56	0.84136448	223668					
11147	10090.ENSMUSP00000025642	Q99KP6	Prpf19		PRP19/PSO4 pre-mRNA processing factor 19 homolog (S. cerevisiae)	0.00422121	293.837.357	0.69036227	0.34032432	77	8	8.024.675.325	77	0.85089434	741182					
11148	10090.ENSMUSP00000002551	P62315	Snrpd1		small nuclear ribonucleoprotein D1	8,69E+00	31.454.892	0.71927928	0.31791557	75	8	7.170.666.667	75	0.83496237	280594	0.20029795				
11149	10090.ENSMUSP00000001202	Q6NVF0	Ocrl		oculocerebrorenal syndrome of Lowe	0.00721005	27.750.953	0.44330776	0.36034799	69	7	6.320.289.855	69	0.86345421	1396300	0.09738505				
11150	10090.ENSMUSP00000037597	P62317	Snrpd2		small nuclear ribonucleoprotein D2	7,53E+00	314.866.582	0.72432432	0.31759483	75	8	71.88	75	0.83471801	297690	0.20191011				
11151	10090.ENSMUSP00000019362	Q60838	Dvl2		dishevelled 2, dsh homolog (Drosophila)	0.0117699	274.523.507	0.34630631	0.36426753	75	8	6.085.333.333	75	0.86575115	922190	0.08817391				
11152	10090.ENSMUSP00000105709	Q61380	Calm1		calmodulin 1	0.01944196	287.992.376	0.0961039	0.34723141	56	8	3.289.285.714	56	0.85539048	1417878					
11153	10090.ENSMUSP00000099488	P27048	Snrpb		small nuclear ribonucleoprotein B	8,93E+00	314.485.388	0.70631579	0.3179798	76	8	71.0	76	0.83501124	305796	0.19832402				
11410	10090.ENSMUSP00000023462	P63085	Mapk1	Mapk1	mitogen-activated protein kinase 1	0.02438013	27.064.803	0.12684145	0.36948357	90	8	3.918.888.889	90	0.86873228	3462724					
11154	10090.ENSMUSP00000030404	Q9QZH3	Ppie		peptidylprolyl isomerase E (cyclophilin E)	0.01420515	285.387.548	0.63386076	0.35040071	80	7	78.425	80	0.85739419	1261056					
13459	10090.ENSMUSP00000029270	P51943	Ccna2	Ccna2	cyclin A2	0.00323864	289.771.283	0.40092166	0.34509976	63	8	5.988.888.889	63	0.85402209	447402					
13971	10090.ENSMUSP00000068530	Q6PFD9	Nup98	Nup98	nucleoporin 98	0.00212911	301.143.583	0.52308591	0.33206751	59	8	6.430.508.475	59	0.84527417	539728	0.1509509				
11155	10090.ENSMUSP00000036384	Q05144	Rac2		RAS-related C3 botulinum substrate 2	0.00222073	305.146.125	0.24016939	0.32771185	58	8	3.767.241.379	58	0.84219529	246790					
11412	10090.ENSMUSP00000015892	Q922U1	Prpf3	Prpf3	PRP3 pre-mRNA processing factor 3 homolog (yeast)	0.00320772	323.379.924	0.8960452	0.30923379	60	8	7.748.333.333	60	0.82816929	390900	0.25151515				
11156	10090.ENSMUSP00000024739	P11499	Hsp90ab1		heat shock protein 90 alpha (cytosolic), class B member 1	0.01383563	269.440.915	0.11373261	0.37113888	58	7	3.586.206.897	58	0.86966083	741282	0.04994469				
13973	10090.ENSMUSP00000066789	B2RWS6	Ep300	Ep300	E1A binding protein p300	0.02885933	261.817.027	0.22727273	0.38194613	89	7	53.0	89	0.87552536	2513792	0.06743003				
11157	10090.ENSMUSP00000034742	P30276	Ccnb2		cyclin B2	0.00161142	311.181.703	0.40225989	0.32135566	60	8	4.833.333.333	60	0.83755254	287020	0.12923351				
11414	10090.ENSMUSP00000107576	Q91Y86	Mapk8	Mapk8	mitogen-activated protein kinase 8	0.0125412	275.285.896	0.10168651	0.36325871	64	8	35.859.375	64	0.8651647	893882					
12694	10090.ENSMUSP00000023507	Q9WV60	Gsk3b	Gsk3b	glycogen synthase kinase 3 beta	0.02862611	255.717.916	0.21880342	0.3910559	91	7	6.527.472.527	91	0.88021699	3658502					
11158	10090.ENSMUSP00000059501	O70404	Vamp8		vesicle-associated membrane protein 8	0.00415	28.703.939	0.52406134	0.34838424	62	7	5.493.548.387	62	0.85612355	720590	0.09792421				
11159	10090.ENSMUSP00000075614	Q3ULL6	Upf3b		UPF3 regulator of nonsense transcripts homolog B (yeast)	0.00126633	291.359.593	0.65648148	0.34321849	81	8	7.749.382.716	81	0.85280031	415488	0.14141209				
11672	10090.ENSMUSP00000111457	Q9D2G5	Synj2	Synj2	synaptojanin 2	0.00241751	287.801.779	0.61959184	0.34746137	50	8	71.94	50	0.85553709	700058	0.1242487				
12952	10090.ENSMUSP00000096549	P70372	Elavl1	Elavl1	ELAV (embryonic lethal, abnormal vision)-like 1 (Hu antigen R)	0.0056937	305.972.046	0.80054274	0.32682724	67	7	7.653.731.343	67	0.84155996	478074					
11160	10090.ENSMUSP00000020397	P62320	Snrpd3		small nuclear ribonucleoprotein D3	0.00135528	314.358.323	0.67266067	0.31810833	78	8	6.926.923.077	78	0.83510898	398212	0.19348947				
11161	10090.ENSMUSP00000100599	A0A0N4SUH6	ENSMUSG00000078184		RIKEN cDNA B020018G12 gene	0.00133476	291.232.529	0.64378199	0.34336824	82	8	7.682.926.829	82	0.85289805	427026	0.13994402				
11162	10090.ENSMUSP00000034560	Q7TNP2	Ppp2r1b		protein phosphatase 2 (formerly 2A), regulatory subunit A (PR 65), beta isoform	0.00496167	26.639.136	0.37400821	0.37538755	86	8	683.255.814	86	0.87200665	1398022	0.09158925				
11419	10090.ENSMUSP00000023829	P39689	Cdkn1a	Cdkn1a	cyclin-dependent kinase inhibitor 1A (P21)	0.0038623	278.462.516	0.41885522	0.35911476	55	8	6.825.454.545	55	0.86272114	402266	0.10323202				
11163	10090.ENSMUSP00000058757	P35235	Ptpn11		protein tyrosine phosphatase, non-receptor type 11	0.00598659	281.448.539	0.33333333	0.35530474	66	8	6.422.727.273	66	0.8604242	1043664					
11164	10090.ENSMUSP00000030348	P61327	Magoh		mago-nashi homolog, proliferation-associated (Drosophila)	0.00133476	291.232.529	0.64378199	0.34336824	82	8	7.682.926.829	82	0.85289805	427026	0.13994402				
11165	10090.ENSMUSP00000052262	P70280	Vamp7		vesicle-associated membrane protein 7	0.00356242	287.611.182	0.52022529	0.34769163	63	7	5.479.365.079	63	0.85568371	719486	0.09802084				
11166	10090.ENSMUSP00000021283	Q5SW28	Pik3r5		phosphoinositide-3-kinase, regulatory subunit 5, p101	0.00226015	293.074.968	0.32670807	0.34120962	70	8	4.852.857.143	70	0.85148079	576626	0.10216541				
12703	10090.ENSMUSP00000014911	P29037	Tbp	Tbp	TATA box binding protein	0.00538337	294.917.408	0.4039548	0.33907798	60	8	53.6	60	0.85006353	692166	0.11308017				
11167	10090.ENSMUSP00000085867	Q99M28	Rnps1		ribonucleic acid binding protein S1	0.00260091	290.914.867	0.64119894	0.34374318	83	8	763.373.494	83	0.85314241	515008					
13984	10090.ENSMUSP00000044548	Q9CWZ3	Rbm8a	Rbm8a	RNA binding motif protein 8a	0.00133476	291.232.529	0.64378199	0.34336824	82	8	7.682.926.829	82	0.85289805	427026	0.13994402				
11168	10090.ENSMUSP00000062864	Q9JHG7	Pik3cg		phosphoinositide-3-kinase, catalytic, gamma polypeptide	0.00168898	292.757.306	0.34464043	0.34157986	67	8	5.043.283.582	67	0.85172515	460324					
11169	10090.ENSMUSP00000023165	P45481	Crebbp		CREB binding protein	0.01388103	279.606.099	0.25282678	0.35764599	67	8	4.840.298.507	67	0.86184146	1287640	0.08000493				
11170	10090.ENSMUSP00000101315	O35904	Pik3cd		phosphatidylinositol 3-kinase catalytic delta polypeptide	0.00164596	292.566.709	0.35123615	0.34180239	69	8	5.036.231.884	69	0.85187176	457642					
13475	10090.ENSMUSP00000091495	P25322	Ccnd1	Ccnd1	cyclin D1	0.00896271	278.526.048	0.33710407	0.35903285	52	8	6.409.615.385	52	0.86267227	640920					
11171	10090.ENSMUSP00000105663	P34152	Ptk2		PTK2 protein tyrosine kinase 2	0.01130507	292.884.371	0.27536232	0.34143167	70	8	4.922.857.143	70	0.85162741	2451752	0.09690664				
11172	10090.ENSMUSP00000009774	P62715	Ppp2cb		protein phosphatase 2 (formerly 2A), catalytic subunit, beta isoform	0.01009114	265.628.971	0.34236874	0.37646496	91	8	6.686.813.187	91	0.8725931	1804654					
11173	10090.ENSMUSP00000007130	Q02248	Ctnnb1		catenin (cadherin associated protein), beta 1	0.02386475	263.024.142	0.22215692	0.38019324	83	7	6.107.228.916	83	0.87459681	2077324	0.07750953				
11174	10090.ENSMUSP00000006565	Q9JJ66	Cdc20		cell division cycle 20	0.00426761	281.702.668	0.40905084	0.35498421	83	8	6.178.313.253	83	0.86022872	785764					
11175	10090.ENSMUSP00000070728	Q3ULA2	Btrc		beta-transducin repeat containing protein	0.00491211	291.550.191	0.42721519	0.34299412	80	8	59.75	80	0.8526537	593506	0.11534749				
12199	10090.ENSMUSP00000088837	P15208	Insr	Insr	insulin receptor	0.00582887	287.420.584	0.30745098	0.34792219	51	7	5.803.921.569	51	0.85583032	773294	0.11161388				
11176	10090.ENSMUSP00000071989	P24860	Ccnb1		cyclin B1	0.00403887	288.945.362	0.35211268	0.34608619	72	8	5.665.277.778	72	0.85465741	706252	0.10171055				
13993	10090.ENSMUSP00000051544	O70480	Vamp4	Vamp4	vesicle-associated membrane protein 4	0.00634589	290.914.867	0.52994555	0.34374318	58	8	5.653.448.276	58	0.85314241	880600	0.1020478				
11177	10090.ENSMUSP00000086312	Q8R0A0	Gtf2f2		general transcription factor IIF, polypeptide 2	8,39E+00	310.228.717	0.58146067	0.32234282	89	8	6.482.022.472	89	0.8382856	211682	0.18005618				
11178	10090.ENSMUSP00000133154	E9PV04	Gm8994		predicted gene 8994	0.00597221	289.898.348	0.54603175	0.3449485	91	8	7.079.120.879	91	0.85392435	1073974					
13995	10090.ENSMUSP00000030797	P63024	Vamp3	Vamp3	vesicle-associated membrane protein 3	0.00493318	287.865.311	0.55584416	0.34738468	56	7	5.794.642.857	56	0.85548822	720098	0.10403309				
11179	10090.ENSMUSP00000021273	P63044	Vamp2		vesicle-associated membrane protein 2	0.01025809	278.970.775	0.40677321	0.35846049	73	7	5.093.150.685	73	0.86233017	1102946	0.078598				
11180	10090.ENSMUSP00000034296	O08908	Pik3r2		phosphatidylinositol 3-kinase, regulatory subunit, polypeptide 2 (p85 beta)	0.00314944	290.533.672	0.31442242	0.34419418	77	8	4.812.987.013	77	0.85343564	717648	0.0988293				
13228	10090.ENSMUSP00000020099	P11440	Cdk1	Champ1	cyclin-dependent kinase 1	0.01424783	270.139.771	0.24511082	0.37017874	118	8	5.008.474.576	118	0.86912325	1643918	0.07175465				
11181	10090.ENSMUSP00000004990	Q9QZ80	Mapk14		mitogen-activated protein kinase 14	0.02259679	274.015.248	0.13584475	0.36494319	73	8	3.591.780.822	73	0.86614212	1423324					
11182	10090.ENSMUSP00000026667	Q91VC3	Eif4a3		eukaryotic translation initiation factor 4A3	0.00597221	289.898.348	0.54603175	0.3449485	91	8	7.079.120.879	91	0.85392435	1073974					
13999	10090.ENSMUSP00000030642	Q9R1P3	Psmb2	Psmb2	proteasome (prosome, macropain) subunit, beta type 2	0.00489816	277.128.335	0.52387042	0.36084365	69	7	6.997.101.449	69	0.86374743	1002188					
11183	10090.ENSMUSP00000031583	E9Q4Z2	Acacb		acetyl-Coenzyme A carboxylase beta	0.03031524	29.523.507	0.06628622	0.33871315	68	7	2.029.411.765	68	0.84981918	3322922					
11184	10090.ENSMUSP00000002733	Q3THK3	Gtf2f1		general transcription factor IIF, polypeptide 1	0.00142969	309.339.263	0.54825609	0.32326967	92	8	6.333.695.652	92	0.8389698	260862	0.17164487				
11185	10090.ENSMUSP00000020843	Q705X9	Acaca		acetyl-Coenzyme A carboxylase alpha	0.03170336	296.886.912	0.06606991	0.33682859	69	7	1.963.768.116	69	0.84854853	3438912					
12209	10090.ENSMUSP00000000137	P61161	Actr2	Actr2	ARP2 actin-related protein 2	0.00332206	279.606.099	0.56240929	0.35764599	53	8	6.390.566.038	53	0.86184146	276610					
11186	10090.ENSMUSP00000031697	Q9WTX6	Cul1		cullin 1	0.00387858	292.503.177	0.40336808	0.34187663	87	8	5.854.022.989	87	0.85192063	730568					
11187	10090.ENSMUSP00000038744	Q9WTX5	Skp1a		S-phase kinase-associated protein 1A	0.00674441	287.102.922	0.38815117	0.34830715	89	8	5.868.539.326	89	0.85607468	859696	0.10608123				
11188	10090.ENSMUSP00000045487	Q9CR99	ENSMUSG00000036463		RIKEN cDNA 4930544G11 gene	0.01495758	270.330.368	0.19845679	0.36991774	81	8	4.860.493.827	81	0.86897664	1640570	0.06722675				
11189	10090.ENSMUSP00000033154	Q07832	Plk1		polo-like kinase 1	0.01025227	270.775.095	0.32258772	0.36931018	96	8	5.752.083.333	96	0.86863454	1173074					
11190	10090.ENSMUSP00000029653	P01132	Egf		epidermal growth factor	0.01532933	26.111.817	0.2912377	0.38296837	94	8	5.942.553.191	94	0.87606295	1944182	0.07481644				
11191	10090.ENSMUSP00000026572	Q61411	Hras1		Harvey rat sarcoma virus oncogene 1	0.00993141	265.057.179	0.23071161	0.37727709	90	8	5.701.111.111	90	0.87303294	1663234					
11192	10090.ENSMUSP00000021698	P07901	Hsp90aa1		heat shock protein 90, alpha (cytosolic), class A member 1	0.0321659	251.397.713	0.13089133	0.39777609	91	7	4.595.604.396	91	0.88354022	2230398	0.05083633				
11193	10090.ENSMUSP00000023460	Q9CQ49	Ncbp2		nuclear cap binding protein subunit 2	0.00417366	285.387.548	0.48151606	0.35040071	104	7	6.696.153.846	104	0.85739419	869294	0.11686132				
11194	10090.ENSMUSP00000051619	Q63844	Mapk3		mitogen-activated protein kinase 3	0.02114768	270.711.563	0.12844933	0.36939686	91	8	3.821.978.022	91	0.86868341	3069558					

11195	10090.ENSMUSP00000043204	P62876	Polr2l		polymerase (RNA) II (DNA directed) polypeptide L	0.00512912	27.566.709	0.44669436	0.3627564	108	7	6.709.259.259	108	0.86487147	1249634	0.10353795
11196	10090.ENSMUSP00000023036	P62878	Rbx1		ring-box 1	0.01142002	272.808.132	0.28680397	0.36655799	115	7	6.122.608.696	115	0.86707067	1559886	0.08884962
11197	10090.ENSMUSP00000007708	Q76MZ3	Ppp2r1a		protein phosphatase 2 (formerly 2A), regulatory subunit A (PR 65), alpha isoform	0.02307964	252.668.361	0.23147107	0.39577571	127	8	6.048.818.898	127	0.8825628	3844122	
12221	10090.ENSMUSP00000094225	Q9Z0Z3	Skp2	Skp2	S-phase kinase-associated protein 2 (p45)	0.00144771	305.463.787	0.55133424	0.32737105	67	8	6.155.223.881	67	0.84195093	246860	0.14551357
12477	10090.ENSMUSP00000030464	Q64143	Pik3r3	Pik3r3	phosphatidylinositol 3 kinase, regulatory subunit, polypeptide 3 (p55)	0.00215261	29.364.676	0.33695161	0.34054522	67	8	488.358.209	67	0.85104095	565200	0.10412755
11198	10090.ENSMUSP00000079380	P63001	Rac1		RAS-related C3 botulinum substrate 1	0.01704978	275.540.025	0.16404582	0.36292368	102	8	3.787.254.902	102	0.86496921	1292500	
11199	10090.ENSMUSP00000001780	P31750	Akt1		thymoma viral proto-oncogene 1	0.03418171	262.198.221	0.13962264	0.38139084	106	7	4.398.113.208	106	0.87523214	2679608	
12479	10090.ENSMUSP00000056774	P26450	Pik3r1	Pik3r1	phosphatidylinositol 3-kinase, regulatory subunit, polypeptide 1 (p85 alpha)	0.00649973	283.989.835	0.24036281	0.35212528	99	8	4.326.262.626	99	0.85846936	1068604	0.082405
11200	10090.ENSMUSP00000019882	P60898	Polr2i		polymerase (RNA) II (DNA directed) polypeptide I	0.00515223	279.606.099	0.40179462	0.35764599	119	7	642.605.042	119	0.86184146	1364972	0.10534509
11968	10090.ENSMUSP00000005164	P68181	Prkacb	Prkacb	protein kinase, cAMP dependent, catalytic, beta	0.01162591	284.371.029	0.12039743	0.35165326	59	8	3.069.491.525	59	0.85817613	1086400	
11201	10090.ENSMUSP00000021090	Q60631	Grb2		growth factor receptor bound protein 2	0.01486067	257.560.356	0.25954962	0.38825851	110	8	5.608.181.818	110	0.87879973	2528764	
11969	10090.ENSMUSP00000005606	P05132	Prkaca	Prkaca	protein kinase, cAMP dependent, catalytic, alpha	0.01716131	274.904.701	0.1347649	0.36376242	74	8	3.371.621.622	74	0.86545792	1528522	
11202	10090.ENSMUSP00000093980	P62488	Polr2g		polymerase (RNA) II (DNA directed) polypeptide G	0.00526422	279.034.307	0.39733894	0.35837887	120	7	6.398.333.333	120	0.8622813	1392122	0.10386905
11203	10090.ENSMUSP00000015800	Q3U9G0	Hspa8		heat shock protein 8	0.0412094	260.038.119	0.31771918	0.384559	132	7	6.366.666.667	132	0.87689375	3700956	
11204	10090.ENSMUSP00000031167	Q8CFI7	Polr2b		polymerase (RNA) II (DNA directed) polypeptide B	0.00583807	278.398.983	0.38707492	0.35919671	122	7	6.343.442.623	122	0.86277001	1450598	0.10182091
12996	10090.ENSMUSP00000044305	Q9DC48	Cdc40	Cdc40	cell division cycle 40	0.00132521	323.443.456	0.82813207	0.30917305	67	8	7.474.626.866	67	0.82812042	449788	0.24506973
11205	10090.ENSMUSP00000051968	Q63871	Polr2k		polymerase (RNA) II (DNA directed) polypeptide K	0.00760569	271.791.614	0.37380645	0.36792894	125	7	62.768	125	0.8678526	1707854	0.09285207
11206	10090.ENSMUSP00000104298	P02340	Trp53		transformation related protein 53	0.06186778	253.875.476	0.1137931	0.39389389	116	8	4.556.034.483	116	0.88163425	5271798	0.05312399
11718	10090.ENSMUSP00000020329	Q01279	Egfr	Egfr	epidermal growth factor receptor	0.02240689	252.604.828	0.23032714	0.39587525	117	8	5.768.376.068	117	0.88261167	3612248	
11207	10090.ENSMUSP00000021405	Q923G2	Polr2h		polymerase (RNA) II (DNA directed) polypeptide H	0.00846493	269.949.174	0.36085138	0.3704401	128	7	6.209.375	128	0.86926987	2007212	0.08999094
11208	10090.ENSMUSP00000090237	P05480	Src		Rous sarcoma oncogene	0.02501912	264.485.388	0.19726324	0.37809272	122	7	4.726.229.508	122	0.87347278	2770128	0.06526809
11209	10090.ENSMUSP00000004786	Q80UW8	Polr2e		polymerase (RNA) II (DNA directed) polypeptide E	0.00858668	269.885.642	0.35719477	0.37052731	129	7	6.180.620.155	129	0.86931874	2032908	0.08957421
11210	10090.ENSMUSP00000043566	P61219	Polr2f		polymerase (RNA) II (DNA directed) polypeptide F	0.01795603	266.581.957	0.31418597	0.37511916	138	7	5.835.507.246	138	0.87186003	2469596	0.08104871
11211	10090.ENSMUSP00000080543	D3YYZ2	Gm5239		predicted pseudogene 5239	0.07577783	236.340.534	0.10805452	0.42311828	270	7	4.564.814.815	270	0.89512267	10281420	

Supplementary Table S5. A focus on PPI network hubs

SUID	Database Identifier	Canonical Name	Name	Description	Average Shortest Path Length	Betweenness Centrality	Closeness Centrality	Clustering Coefficient	Degree	Eccentricity	Neighborhood Connectivity	Number Of Undirected Edges	Query Term	Radiality	Topological Coefficient
11212	10090.ENSMUSP0000013679 1	J3QK04	Gm7808	predicted pseudogene 7808	236.340.534	0.07577783	0.42311828	0.10805452	270	7	4.564.814.815	270		0.89512267	0.04686668
12018	10090.ENSMUSP0000011418 0	Q9ET24	Ubc	ubiquitin C	240.025.413	0.05482875	0.41662255	0.12827787	235	7	4.778.297.872	235	Ubc	0.89228814	0.04982584
11206	10090.ENSMUSP0000010429 8	P02340	Trp53	transformation related protein 53	253.875.476	0.06186778	0.39389389	0.1137931	116	8	4.556.034.483	116		0.88163425	0.05312399
11211	10090.ENSMUSP0000008054 3	D3YYZ2	Gm5239	predicted pseudogene 5239	236.340.534	0.07577783	0.42311828	0.10805452	270	7	4.564.814.815	270		0.89512267	

Supplementary Table S6. DEGs deregulated in *Cx30*$^{-/-}$ sorted in ascending order of fold change (FC).

Probe name, gene symbol, description and FC are shown in this table for each one of the 57 out 81 DEGs that encode 56 proteins.

ProbeName	GeneSymbol	Description	FC
A_55_P2934160	*Gjb6*	Mus musculus gap junction protein – Transcript variant 3	-85.6744
A_52_P482251	*Gjb6*	Mus musculus gap junction protein – Transcript variant 2	-5.46416
A_51_P502906	*Ang4*	Angiogenin, ribonuclease A family, member 4(Ang4)	-4.51398
A_52_P560996	*Gm26782*	Mus musculus adult male colon cDNA	-4.25546
A_52_P98778	*Ang4*	Angiogenin, ribonuclease A family, member 4(Ang4)	-3.39696
A_52_P91019	*Olfr1386*	Mus musculus olfactory receptor 1386 (Olfr1386)	-2.84102
A_52_P382886	*Gjb2*	Mus musculus gap junction protein	-2.81565
A_55_P2030667	*Eda*	Mus musculus ectodysplasin-A (Eda)	-2.77284
A_51_P338031	*Trpm1*	Mus musculus transient receptor potential cation channel	-2.68726
A_51_P230537	*Ccdc114*	Mus musculus coiled-coil domain containing 114 (Ccdc114)	-2.51915
A_52_P277082	*Gpr143*	Mus musculus G protein-coupled receptor 143 (Gpr143)	-2.43662
A_52_P680761	*Tdrd6*	Mus musculus tudor domain containing 6 (Tdrd6)	-2.34165
A_51_P485985	*Mbnl3*	Mus musculus muscleblind-like 3 (Drosophila) (Mbnl3)	-2.31374
A_51_P144024	*Trpa1*	Mus musculus transient receptor potential cation channel	-2.29293
A_65_P11062	*Gm36463*	PREDICTED: Mus musculus predicted gene	-2.27591
A_55_P2173952	*Myh6*	Mus musculus myosin	-2.24038
A_55_P2716656	*Pgd*	phosphogluconate dehydrogenase [Source:MGI Symbol]	-2.23892
A_55_P2924285	*Dusp14*	dual specificity phosphatase 14 [Source:MGI Symbol]	-2.21072
A_66_P137343	*Enpp6*	Mus musculus 0 day neonate head cDNA	-2.21023
A_52_P208416	*Olfr1431*	Mus musculus olfactory receptor 1431 (Olfr1431)	-2.19804
A_66_P105262	*Hspb11*	PREDICTED: Mus musculus heat shock protein family B (small)	-2.07118
A_55_P2714597	*Bhmt*	Mus musculus betaine-homocysteine methyltransferase (Bhmt)	-2.05747
A_55_P2483194	*Wfdc18*	Mus musculus WAP four-disulfide core domain 18 (Wfdc18)	-2.04821
A_52_P556462	*Fancd2*	Mus musculus Fanconi anemia	-2.03914
A_55_P2824451	*Fam167a*	Mus musculus family with sequence similarity 167	-2.00453
A_51_P201751	*Olfr870*	Mus musculus olfactory receptor 870 (Olfr870)	-1.89078
A_51_P100625	*Apon*	Mus musculus apolipoprotein N (Apon)	-1.88786
A_55_P2716491	*Ang6*	Mus musculus angiogenin	-4.3259
A_51_P391159	*Ang*	angiogenin, ribonuclease, RNase A family, 5	-3.3733
A_66_P132845	*Prg3*	Mus musculus proteoglycan 3 (Prg3)	-3.1445
A_52_P25420	*Srcin1*	Mus musculus SRC kinase signaling inhibitor 1 (Srcin1)	-2.4185

A_55_P2180949	*Lcp2*	lymphocyte cytosolic protein 2 [Source:MGI Symbol	-2.2661
A_55_P2737912	*Lgi3*	Mus musculus 10 days neonate medulla oblongata cDNA	-2.1291
A_55_P2743344	*Svil*	supervillin [Source:MGI Symbol]	1.73276
A_51_P321610	*Mapkbp1*	Mus musculus mRNA for JNK-binding protein JNKBP1	2.36026
A_66_P103780	*Gm3646*	Mus musculus predicted gene 3646 (Gm3646)	2.80451
A_55_P2735845	*Tnfrsf10b*	tumor necrosis factor receptor superfamily, member 10b [Source:MGI Symbol]	3.05238
A_55_P2069765	*Kiss1*	Mus musculus KiSS-1 metastasis-suppressor (Kiss1)	1.678236
A_51_P309854	*Kcnn2*	Mus musculus potassium intermediate/small conductance calcium-activated channel	1.688343
A_52_P127572	*Elf4*	Mus musculus E74-like factor 4 (ets domain transcription factor) (Elf4)	1.731594
A_55_P2720113	*Pamr1*	peptidase domain containing associated with muscle regeneration 1 [Source:MGI Symbol]	1.874715
A_66_P110610	*Clcnkb*	Mus musculus chloride channel Kb (Clcnkb)	2.040674
A_55_P2740248	*Pkd1*	Mus musculus cDNA	2.050697
A_55_P2208300	*Zfp950*	PREDICTED: Mus musculus RIKEN cDNA 5830428H23 gene (5830428H23Rik)	2.078884
A_55_P2715301	*Reln*	reelin [Source:MGI Symbol	2.167367
A_55_P1984881	*Fyb2*	FYN binding protein 2	2.385044
A_52_P160418	*Ubr3*	Mus musculus ubiquitin protein ligase E3 component n-recognin 3 (Ubr3)	2.454792
A_55_P2783542	*Rasgrf2*	Mus musculus RAS protein-specific guanine nucleotide-releasing factor 2 (Rasgrf2)	2.465768
A_55_P2010811	*Olfr59*	Mus musculus olfactory receptor 59 (Olfr59)	2.492033
A_51_P134923	*Rnf148*	Mus musculus ring finger protein 148 (Rnf148)	2.560107
A_55_P2804650	*Il1r2*	Mus musculus interleukin 1 receptor	2.731522
A_52_P161411	*Usp4*	ubiquitin specific peptidase 4 (proto-oncogene) [Source:MGI Symbol]	2.751463
A_55_P1996893	*Zpbp2*	Mus musculus zona pellucida binding protein 2 (Zpbp2)	2.767583
A_55_P2040873	*Gm867*	Mus musculus predicted gene 867 (Gm867)	2.901609
A_66_P130275	*Gm4491*	PREDICTED: Mus musculus predicted gene 4491 (Gm4491)	2.918621
A_52_P565847	*AU018091*	Mus musculus expressed sequence AU018091 (AU018091)	3.147764
A_51_P464703	*Ccl8*	Mus musculus chemokine (C-C motif) ligand 8 (Ccl8)	3.506606
A_55_P2737692	*Npy1r*	Mus musculus neuropeptide Y receptor Y1 (Npy1r)	3.697697

Supplementary Table S7. DEGs belonging to the pair comparison Cx30wt vs Cx30KO. Information about feature type, description and regulation are shown in the table for each of the 15 out 81 DEGs that encode different types of non-coding RNAs.

Feature Type	Description	Regulation
lincRNA	lincRNA:chr4:98943050-98959998 forward strand	up
lincRNA	lincRNA:chr1:175660642-175671878 reverse strand	up
lincRNA	lincRNA:chr6:131263850-131314850 reverse strand	up
lincRNA	lincRNA:chr4:53312709-53355184 forward strand	down
lincRNA	lincRNA:chr15:58327703-58329443 reverse strand	down
lincRNA	lincRNA:chr6:31037606-31037912 reverse strand	up
lincRNA	lincRNA:chr2:104590593-104606218 forward strand	up
lincRNA	lincRNA:chrX:133315875-133338600 reverse strand	up
ncRNA	A930018M24Rik - Mus musculus adult male diencephalon cDNA	up
antisense lncRNA	B230369F24Rik - Mus musculus adult pancreas islet cells cDNA	up
antisense lncRNA	9530036O11Rik - Mus musculus RIKEN cDNA 9530036O11Rik	up
lncRNA	Gm33951 - PREDICTED: Mus musculus predicted gene	down
ncRNA	Gm14169 - Mus musculus predicted gene 14169	up
ncRNA	Gm13429 - Mus musculus 0 day neonate lung cDNA	up
lncRNA	Gm20098 - Mus musculus predicted gene	down

Supplementary Table S8. Correlation between deregulated miRNAs and predicted/ validated deregulated miRNA targets. The table shows that only one pair of miRNA/mRNA has an inverse correlation between expression levels (up vs down), i.e. mmu-miR-29b-3p and *Gjb2*.

$Cx30^{wt}$ vs $Cx30^{ko}$

Deregulated miRNAs	Regulation	DEGs	Regulation
mmu-miR-29b-3p	up	*Elf4*	Up
		Pkd1	Up
		AU018091	Up
mmu-miR-34c-5p	up	*Gjb2*	Down
		Elf4	Up
mmu-miR-335-5p	up	*Elf4*	Up
mmu-miR-181a-1-3p	up	*Reln*	Up